# A Higgs-Free Electroweak Model Based on Self-Energy and a Composite Neutral Sector

**Hyoyoung Choi**[1]*

**1** Independent Researcher, Gunsan, Republic of Korea.

* E-mail: 7icarus7@gmail.com

## Abstract

**The Higgs mechanism is accompanied by several well-known conceptual difficulties, including the arbitrariness of Yukawa couplings, the hierarchy problem, and vacuum energy concerns associated with the vacuum expectation value of the Higgs field. Motivated by these issues, this paper proposes a Higgs-free electroweak model in which mass is reinterpreted in terms of self-energy and composite dynamics rather than through a fundamental Higgs mechanism. In this picture, the charged weak-boson sector is organized through self-energy mass generation, while the neutral massive sector is reorganized as a composite spectrum. The observed $Z^0$ boson and the 125 GeV scalar resonance $X_1^0(125)$ are interpreted, respectively, as the vector ground state and the first excited scalar state of an underlying $W^+W^-$ system. Stückelberg compensating fields organize the massive weak-vector sector in a gauge-compatible representation and parameterize its longitudinal degrees of freedom. The framework separates the high-energy behavior into two regimes. A finite-formation principle controls the TeV-scale longitudinal weak-boson response, while the KGC mechanism strongly suppresses trans-Planckian propagation. At the effective level, these ingredients define a minimal Higgs-free electroweak Lagrangian architecture describing the charged weak sector with a self-energy-generated mass scale, the Stückelberg compensating structure, the composite neutral sector, and KGC-dressed high-energy propagation. The principal phenomenological tests are precision neutral-current observables and asymmetries, the production and decay properties of $X_1^0(125)$, vector-boson scattering, and searches for an additional neutral resonance in the 133.7–138.2 GeV interval. The present construction defines a testable first-stage Higgs-free replacement model that provides a concrete alternative mechanism for electroweak mass organization and neutral spectroscopy, while the complete chiral and non-Abelian realization is left to a subsequent stage.**

## Contents

**1 Introduction** **1**

**2 Mass Generation from Self-Energy and First Composite Electroweak Results** **4**
2.1 Mass from Fundamental Source-Charge Self-Energies 4
2.2 Charged Weak-Boson Self-Energy Scale 7
2.3 Composite Interpretation of $Z^0$ and $X_1^0(125)$ 8
2.4 Effective Binding Dynamics of the Neutral $W^+W^-$ Sector 11
2.5 A Radial-Excitation Prediction of an Additional Neutral Resonance Near 135.4 GeV 13
2.6 Mass-Eigenstate Effective-Coupling Parameterization of $X_1^0(125)$ 15

**3 Physical Organization of the Higgs-Free Electroweak Model** **17**
3.1 Charge Self-Energy as the Primary Mass Origin in the Present Framework 18
3.2 Vacuum Energy, Spacetime Curvature, and the Higgs Vacuum 19
3.3 Reframing the Electroweak Mass Problem 22

**4 Stückelberg Gauge Structure Without a Fundamental Higgs Condensate** **23**
4.1 Abelian Stückelberg Prototype 23
4.2 Charged Weak-Sector Prototype and Non-Abelian Completion 24
4.3 Role and Scope of the Stückelberg Layer 25

**5 High-Energy Consistency and the TeV-Scale Longitudinal Issue** **26**
5.1 A Finite-Formation Suppression Ansatz Motivated by Time–Energy Uncertainty 26
5.2 KGC Ultraviolet Suppression and the Route Toward Perturbative Completion 30
5.3 Layered High-Energy Consistency Structure 32

**6 Minimal Effective Self-Energy Framework** **33**
6.1 Schematic Effective Lagrangian Architecture 33
6.2 Effective Couplings of the Composite Neutral Sector 34
6.3 Scope of the Effective Construction 36

**7 Phenomenological Tests and Falsifiability** **36**
7.1 Precision Neutral-Current Constraints 36
7.2 Signal Strengths of the $X_1^0(125)$ Scalar Resonance 37
7.3 Search Window for an Additional Neutral Resonance Near 135.4 GeV 38
7.4 Vector-Boson Scattering 38
7.5 Scope of the First-Stage Construction 39

**8 Conclusion** **39**

**A Illustrative Quark-Scale Mapping of the Self-Energy Ansatz** **41**
A.1 Electrostatic Effective Length Scales 42
A.2 An Extended Phenomenological Ansatz with a Strong-Sector Term 42

**B Wave-Packet Overlap Benchmark for the Neutral-State Width Hierarchy** **44**

**C Formation-Time Consistency of the Composite Interpretation** **45**

**References** **46**

# 1 Introduction

The electroweak sector of the Standard Model is one of the most successful structures in modern particle physics. The unified gauge description developed by Glashow, Weinberg, and Salam provides an accurate account of weak and electromagnetic interactions [1–3]. The discovery of weak neutral currents, the charged weak bosons $W^{\pm}$, and the neutral boson $Z^0$ confirmed the characteristic gauge-boson predictions of the electroweak theory [4–8]. The ATLAS and CMS Collaborations later discovered a neutral scalar resonance near 125 GeV, conventionally identified with the Higgs boson [9, 10].

In the electroweak Standard Model, the Brout–Englert–Higgs mechanism (Higgs mechanism) reconciles the gauge structure of the theory with the observed nonzero masses of the weak vector bosons. Spontaneous symmetry breaking in a fundamental scalar sector produces a nonzero vacuum expectation value and generates the $W$- and $Z$-boson masses while preserving the gauge structure of the theory [2,11–13]. Yukawa interactions generate the masses of quarks and charged leptons after electroweak symmetry breaking. Together, the scalar and Yukawa sectors provide the conventional Standard Model description of weak-boson and charged-fermion masses [2,14].

Despite its empirical success, the Higgs mechanism does not by itself determine the deeper microscopic origin of the electroweak scale or the observed fermion-mass hierarchy. Furthermore, the parameters governing the symmetry-breaking scale and the Yukawa couplings governing the fermion masses are introduced as adjustable quantities whose values are fixed a posteriori to reproduce the observed electroweak scale and fermion mass spectrum, rather than predicted by the mechanism itself. Several central explanatory problems therefore remain:

1) **The Higgs potential postulates the electroweak vacuum rather than deriving it.**

   For one complex scalar doublet, gauge invariance and renormalizability permit the scalar potential

   $$V(\Phi) = -\mu^2 \Phi^\dagger \Phi + \lambda \left(\Phi^\dagger \Phi\right)^2 . \tag{1}$$

   The form of this potential is constrained by the Standard Model field content, but the parameters $\mu^2$ and $\lambda$, including the sign that places the minimum away from the symmetric point, are not derived from a deeper electroweak dynamics. Their values are not fixed by the electroweak gauge structure and are determined phenomenologically so that

   $$\Phi^\dagger \Phi = \frac{\mu^2}{2\lambda} \tag{2}$$

   defines a nonzero vacuum expectation value [14,15]. The Higgs mechanism then calculates the consequences of this vacuum configuration; it does not explain why this particular configuration is realized in nature.

2) **The electroweak scale is measured first and identified with the Higgs vacuum scale afterward.**

   The conventional electroweak scale is obtained from the measured Fermi constant,

   $$v = \left(\sqrt{2} G_F\right)^{-1/2} \simeq 246\,\text{GeV}. \tag{3}$$

   The Higgs formulation identifies this empirical scale with the vacuum expectation value of the scalar field. It does not derive $v \simeq 246\,\text{GeV}$ from the gauge structure, from the scalar potential, or from an independent microscopic principle [14,15]. The numerical value of the weak scale is fixed from the measured Fermi constant rather than predicted by the electroweak gauge couplings.

3) **Yukawa couplings reproduce the fermion masses but do not explain their hierarchy.**

   For a charged fermion $f$, the Standard Model gives

   $$m_f = \frac{y_f v}{\sqrt{2}}, \tag{4}$$

   where $y_f$ is an independent Yukawa coupling. Once $m_f$ and $v$ are measured, the equation determines $y_f$; it does not predict the fermion mass. The large hierarchy among

the quark and charged-lepton masses is therefore transferred directly into an equally unexplained hierarchy among the Yukawa couplings [14, 15]. The Higgs mechanism parametrizes the observed fermion spectrum without identifying its physical origin.

4) **The Higgs mechanism generates weak-boson masses but does not derive the scalar mass scale itself.**

The measured scalar mass fixes the quartic coupling through

$$m_h^2 = 2\lambda v^2. \tag{5}$$

Thus the observed value $m_h \simeq 125\,\mathrm{GeV}$ determines $\lambda$ after $v$ is known. The minimal theory does not predict why the scalar resonance has this mass. Within the conventional effective-field-theory naturalness criterion, the scalar mass parameter is radiatively sensitive to physics far above the electroweak scale, giving rise to the hierarchy and naturalness problem that originally motivated dynamical alternatives to a fundamental scalar sector [14, 16].

5) **The minimal renormalizable Standard Model leaves neutrinos massless.**

Its field content contains no right-handed neutrino and no renormalizable mass operator for the active neutrinos. Neutrino oscillations establish nonzero neutrino mass differences, requiring additional fields or higher-dimensional operators beyond the minimal theory [15, 17, 18]. The Higgs mechanism in its minimal Standard Model form therefore does not provide a complete mass-generation framework for the known fermionic sector.

6) **The electroweak Higgs vacuum contributes a vacuum-energy scale approximately $10^{55}$ times larger than the observed dark energy density.**

The nonzero vacuum expectation value required by the Higgs mechanism is accompanied by a nonzero value of the scalar potential at the electroweak minimum. For the conventional normalization $V(0) = 0$,

$$V_{\mathrm{EW}} = -\frac{\lambda v^4}{4} = -\frac{m_h^2 v^2}{8} \simeq -1.2 \times 10^8\,\mathrm{GeV}^4. \tag{6}$$

The observed effective dark energy density is of order [15, 19, 20]

$$\rho_{\mathrm{DE}}^{\mathrm{obs}} \sim 10^{-47}\,\mathrm{GeV}^4, \tag{7}$$

and therefore

$$\frac{|V_{\mathrm{EW}}|}{\rho_{\mathrm{DE}}^{\mathrm{obs}}} \sim 10^{55}. \tag{8}$$

Thus the same Higgs vacuum invoked to generate the electroweak mass scale also introduces a vacuum energy contribution that exceeds the observed cosmological scale by approximately fifty-five orders of magnitude [21].

If the observed dark energy originates from physics outside the Higgs sector, the gravitational effect of $V_{\mathrm{EW}}$ must be cancelled or neutralized while the nonzero Higgs vacuum expectation value is retained. This requires a suppression at the relative level $\frac{\rho_{\mathrm{DE}}^{\mathrm{obs}}}{|V_{\mathrm{EW}}|} \sim 10^{-55}$.

If instead the observed vacuum energy is obtained from the total vacuum sector containing the Higgs contribution, an independent positive contribution must cancel the large negative electroweak term to approximately fifty-five decimal places, leaving only the observed small positive remainder. In either case, the Higgs mechanism requires an additional cancellation mechanism that is not provided by electroweak symmetry breaking itself.

These are not peripheral omissions. The Higgs mechanism successfully relates a chosen scalar vacuum and a set of Yukawa parameters to the measured particle masses, but it does not derive the vacuum scale, the symmetry-breaking parameters, the scalar mass, or the fermion mass hierarchy from a common physical origin. The discovery of the 125 GeV scalar resonance established the existence of a Higgs-like state and its approximately Standard Model-like interactions [9, 10, 22]. It did not directly establish that a fundamental scalar condensate is the microscopic source of all electroweak and fermionic masses.

This explanatory gap provides a concrete reason to investigate a physically different mass-generation framework. The present model assigns mass to self-energy, binding energy, and composite dynamics rather than to a fundamental scalar vacuum. In the present framework, a spatially distributed gauge source is assigned a finite field-energy contribution, and that energy contributes to the inertial mass of the corresponding physical state [23–25]. The neutral massive sector is then organized as a composite $W^+W^-$ spectrum rather than as a fundamental Higgs sector [26].

The framework contains four connected physical elements. First, charge self-energy supplies the mass scale of the charged weak bosons. Second, the observed $Z^0$ boson and the 125 GeV scalar resonance, denoted by $X_1^0(125)$, are treated as low-lying composite channels of an underlying $W^+W^-$ system, with additional neutral excitations expected above them [26]. Third, the already massive charged weak sector is written in a Stückelberg-type gauge-compatible form [27,28]. Fourth, the TeV-scale growth of longitudinal weak-boson amplitudes is controlled by the finite-formation principle developed in this work, while KGC dressing suppresses propagation in the trans-Planckian regime [29–31].

This paper presents the first stage of a Higgs-free electroweak replacement program. The present stage formulates the self-energy origin of the charged weak-boson mass scale, the composite $W^+W^-$ organization of the neutral massive sector, a Stückelberg-compatible representation of the massive charged vectors, and the principal phenomenological tests of these assignments. The complete chiral, flavor, and non-Abelian realization belongs to the subsequent stage of the construction.

## 2 Mass Generation from Self-Energy and First Composite Electroweak Results

### 2.1 Mass from Fundamental Source-Charge Self-Energies

Mass–energy equivalence establishes that every finite contribution to the energy of a localized physical system contributes to its inertial mass [23]. The present framework identifies the self-energies associated with fundamental source charges, together with internal kinetic and binding energies, as the physical origin of the observed rest-energy spectrum [26].

Each fundamental interaction couples to a corresponding source. We denote the electromagnetic, weak, strong, and gravitational source charges by

$$Q_e, \qquad Q_w, \qquad Q_s, \qquad Q_g, \tag{9}$$

respectively. Here the term source charge is used in a unified dynamical sense: it denotes the physical source strength that generates the corresponding interaction field.

For electromagnetism, $Q_e$ is the ordinary electric charge. The weak and strong source charges represent the effective weak and color sources carried by the physical state. For gravity,

the source is the energy–momentum distribution of the system. In the center-of-mass rest frame, the total spatial momentum satisfies

$$P^i = 0. \tag{10}$$

For the rest-frame effective description used here, we define an equivalent scalar gravitational source charge by

$$Q_g(R) \equiv \mathcal{Q}_g\big[T_{\mu\nu}; R\big] \equiv M^{\rm eq}_{\rm grav}(R). \tag{11}$$

The functional $\mathcal{Q}_g[T_{\mu\nu}; R]$ collects the rest-frame energy–momentum content relevant to the gravitational field, including the effects of internal energy, relativistic motion, pressure, and stress. In the weak-field and slow-motion limit,

$$Q_g(R) \longrightarrow M(R), \tag{12}$$

so that the equivalent gravitational charge reduces to the enclosed mass [32].

For an interaction whose effective potential is dominated by an inverse-radius term, the self-energy of a finite source distribution takes the characteristic form

$$U^{(a)}_{\rm self}(R) = \eta_a \beta_a \frac{C_a Q_a^2}{R}, \qquad a \in \{g, e, w, s\}, \tag{13}$$

where $R$ is the characteristic source size, $C_a$ is the interaction coefficient, $\beta_a$ is the structural coefficient determined by the source distribution, and $\eta_a = \pm 1$ specifies the effective attractive or repulsive sign.

The two direct inverse-radius examples are

$$U_{\rm es} = +\beta_e \frac{k_e Q_e^2}{R}, \qquad U_{\rm gs} = -\beta_g \frac{G Q_g^2}{R}. \tag{14}$$

The positive electrostatic sign follows from the repulsive interaction among like electric source elements. The first gravitational contribution,

$$U_{\rm gs}(R) = -\beta_g \frac{G_N Q_g^2}{R}, \tag{15}$$

is the negative attractive self-energy recovered in the Newtonian low-compactness limit.

In the total-GSE framework developed in our preceding work, the equivalent mass associated with gravitational self-energy also participates in the gravitational source. For a finite free-state matter source $M_{\rm fr}$, this gives

$$U_{\rm gs-T}(R) = -\beta_g \frac{G_N M_{\rm fr}^2}{R} + \frac{5}{7}\beta_g^2 \frac{G_N^2 M_{\rm fr}^3}{c^2 R^2} \equiv U_{\rm gs}(R) + U_{\rm m-gs}(R), \tag{16}$$

where the first term is the negative attractive GSE term and the second term is the positive repulsive matter–GSE interaction term [32, 33].

Accordingly, $U_{\rm gs}$ remains the negative attractive contribution, whereas the total quantity $U_{\rm gs-T}$ is negative at low compactness and can become positive when the $R^{-2}$ matter–GSE interaction term dominates at sufficiently high compactness. For the electroweak-scale particle systems considered below, the gravitational compactness is extremely small, and the gravitational contribution therefore reduces effectively to the Newtonian negative term.

For a uniformly charged electric sphere,

$$\beta_e = \frac{3}{5}, \tag{17}$$

giving the standard electrostatic self-energy [24, 25]. The same uniform-profile value may be adopted as a benchmark structural coefficient for other source distributions in the semi-classical estimates below [26].

The weak and strong interactions do not retain a pure $1/R$ form at all scales. Their self-energies are therefore written more generally as

$$U_{\rm ws} = U_{\rm ws}(Q_w, R), \qquad U_{\rm ss} = U_{\rm ss}(Q_s, R), \tag{18}$$

with the inverse-radius expression in Eq. (13) recovered when the relevant short-distance interaction is dominated by a Coulomb-like term. Finite-range, confining, and non-Abelian effects modify the radial dependence and are incorporated through the corresponding effective interaction kernels.

The total source-field self-energy is

$$U_{\rm SE} = U_{\rm gs-T} + U_{\rm es} + U_{\rm ws} + U_{\rm ss}, \tag{19}$$

where $U_{\rm gs-T} \simeq U_{\rm gs}$ in the low-compactness electroweak systems considered below. The rest-energy budget of a localized state is written as

$$mc^2 = U_{\rm SE} + T_{\rm int} + U_{\rm bind} + \cdots, \tag{20}$$

where $T_{\rm int}$ denotes internal kinetic energy and $U_{\rm bind}$ denotes the net binding-energy contribution generated by the internal interactions.

For a composite state formed from constituents with physical masses $m_i$, the corresponding mass relation is

$$Mc^2 = \sum_i m_i c^2 + T_{\rm rel} + U_{\rm bind}^{\rm comp} + \cdots, \tag{21}$$

where the constituent masses already contain their individual self-energy contributions, $T_{\rm rel}$ is their relative kinetic energy, and $U_{\rm bind}^{\rm comp}$ is the total interaction energy of the composite configuration.

Equations (20) and (21) replace the scalar-condensate origin of mass with a direct energy accounting based on fundamental source charges and internal dynamics. In the present framework, charged particles acquire rest energy from the fields generated by their distributed sources, while neutral composite particles retain nonzero masses through constituent self-energies, relative motion, and binding interactions [26].

The same self-energy relation may also be used as an inverse mapping between renormalized quark-mass parameters and effective dressed-source scales. Because this construction does not independently predict the input quark masses, the corresponding numerical illustrations are collected in Appendix A. The main electroweak application begins below with the charged weak-boson sector.

Throughout the phenomenological analysis, $m_W$ and $M_Z$ denote the physical weak-boson pole masses. The notation $M_W^{\rm SE}$ is reserved for the same physical charged-boson mass scale when it appears as the mass parameter of the self-energy effective construction.

## 2.2 Charged Weak-Boson Self-Energy Scale

We now apply the source-energy principle directly to the charged weak boson. This provides an electroweak-scale realization of the proposed self-energy mass mechanism without a fundamental Higgs condensate [26].

The $W^{\pm}$ boson carries electric charge and participates directly in the weak gauge sector. The leading charge-sector estimate in the present framework therefore includes both electromagnetic and effective weak contributions. We first retain the electrostatic term and then introduce a short-distance weak-sector correction.

For a uniformly distributed electric source with $Q_e = \pm e$, the electrostatic self-energy is

$$U_{\rm es}(r) = \beta \frac{\alpha_{\rm em}\hbar c}{r}, \qquad \beta = \frac{3}{5}. \tag{22}$$

Equating this contribution to the measured $W$-boson rest energy gives

$$r_W = \beta \frac{\alpha_{\rm em}\hbar c}{m_W c^2}. \tag{23}$$

Using the PDG 2024 mass input and the benchmark adopted above [15, 26], one obtains

$$m_W = 80.3692\,\mathrm{GeV}/c^2, \qquad \alpha_{\rm em}^{-1} \simeq 137.036, \tag{24}$$

$$r_W \simeq 1.075 \times 10^{-20}\,\mathrm{m}. \tag{25}$$

. This value is the characteristic source scale inferred from Eq. (23), rather than a directly measured hard radius.

As a semi-classical benchmark for the weak-sector contribution, we adopt the repulsive short-distance Yukawa-type self-energy ansatz

$$U_{\rm ws}^{\rm eff}(r) = +\beta \frac{\alpha_W \hbar c}{r} e^{-r/R_W}, \qquad R_W = \frac{\hbar}{m_W c}, \tag{26}$$

where

$$\alpha_W \equiv \frac{g^2}{4\pi}. \tag{27}$$

We use the benchmark value

$$\alpha_W \simeq \frac{1}{29.59} \tag{28}$$

adopted in the preceding analysis [14, 26]. Equation (26) defines the sign and radial form of the effective weak self-energy approximation used here.

For $r \ll R_W$,

$$e^{-r/R_W} = 1 - \frac{r}{R_W} + \mathcal{O}\left(\frac{r^2}{R_W^2}\right), \tag{29}$$

which gives

$$U_{\rm ws}^{\rm eff}(r) \simeq \beta \left[\frac{\alpha_W \hbar c}{r} - \alpha_W m_W c^2\right]. \tag{30}$$

Adding Eqs. (22) and (30), the charged-boson mass relation becomes

$$m_W c^2 = \beta \left[\frac{(\alpha_{\rm em} + \alpha_W)\hbar c}{r'_W} - \alpha_W m_W c^2\right]. \tag{31}$$

The resulting source-radius parameter is

$$r'_W = \frac{\beta\hbar c(\alpha_{\rm em}+\alpha_W)}{m_W c^2(1+\beta\alpha_W)} \simeq 5.93\times10^{-20}\,\mathrm{m}. \tag{32}$$

The corresponding Yukawa range is

$$R_W = \frac{\hbar}{m_W c} \simeq 2.46\times10^{-18}\,\mathrm{m}, \tag{33}$$

and hence

$$\frac{r'_W}{R_W} \simeq 2.42\times10^{-2}, \tag{34}$$

which is consistent with the short-distance expansion used in Eq. (29).

These relations define the finite source-radius parameters associated with the observed $W$-boson mass in the present self-energy mapping [26].

The electrically neutral $Z^0$ exposes a distinct neutral-sector problem for the net-charge version of the same estimate:

$$Q^{(Z)}_{\rm em} = 0 \qquad \Longrightarrow \qquad U^{(Z)}_{\rm es} = 0. \tag{35}$$

Electric neutrality removes the net-charge electrostatic term, but it does not by itself imply that every electroweak self-energy contribution vanishes. The present framework resolves this neutral-sector mass problem by assigning charged internal constituents to the $Z^0$, leading to the $W^+W^-$ composite hypothesis [26].

### 2.3 Composite Interpretation of $Z^0$ and $X^0_1(125)$

We identify the neutral $Z^0$ boson as the lowest $W^+W^-$ composite level and the observed 125 GeV scalar state, denoted here by $X^0_1(125)$, as the next neutral level of the same system [26]. The notation $X^0_n$ is used for the neutral composite excitations above the $Z^0$ ground state, with the subscript $n$ denoting the radial-excitation index $n_r = n$.

The neutral-state masses are written relative to the free two-$W$ threshold as

$$M_Z c^2 = 2m_W c^2 + U^{(Z)}_{\rm binding}, \qquad M_{X_1} c^2 = 2m_W c^2 + U^{(X_1)}_{\rm binding}. \tag{36}$$

Here $U^{(n)}_{\rm binding}$ denotes the net internal energy relative to the free $W^+W^-$ threshold, including relative kinetic and interaction-energy contributions. A negative value places the corresponding level below the two-$W$ threshold.

Using the mutually consistent PDG 2024 central values

$$m_W = 80.3692\,\mathrm{GeV}/c^2, \qquad M_Z = 91.1880\,\mathrm{GeV}/c^2, \qquad M_{X_1} = 125.20\,\mathrm{GeV}/c^2, \tag{37}$$

gives

$$U^{(Z)}_{\rm binding} = M_Z c^2 - 2m_W c^2 = -69.550\,\mathrm{GeV}, \tag{38}$$

$$U^{(X_1)}_{\rm binding} = M_{X_1} c^2 - 2m_W c^2 = -35.538\,\mathrm{GeV}. \tag{39}$$

The two observed neutral states therefore lie substantially below the free $W^+W^-$ threshold in the present constituent bookkeeping [15, 26].

In the first electrostatic binding approximation, we map the net internal energy onto an effective inverse-radius interaction,

$$U_{\text{binding}}^{(a)} = -\frac{\alpha_{\text{em}}\hbar c}{r_a}, \qquad a \in \{Z, X_1\}. \tag{40}$$

The characteristic binding distances are consequently

$$r_Z^0 = \frac{\alpha_{\text{em}}\hbar c}{|U_{\text{binding}}^{(Z)}|} \simeq 2.070 \times 10^{-20}\,\text{m}, \tag{41}$$

and

$$r_{X_1} = \frac{\alpha_{\text{em}}\hbar c}{|U_{\text{binding}}^{(X_1)}|} \simeq 4.052 \times 10^{-20}\,\text{m}. \tag{42}$$

Their ratio is

$$\frac{r_{X_1}}{r_{Z^0}} = \frac{|U_{\text{binding}}^{(Z)}|}{|U_{\text{binding}}^{(X_1)}|} \simeq 1.957 \simeq 2. \tag{43}$$

The common inverse-radius interaction converts the two mass defects directly into an approximately two-to-one hierarchy of characteristic binding distances. This mass-implied structural relation provides the principal geometric organizing clue for the composite interpretation [26].

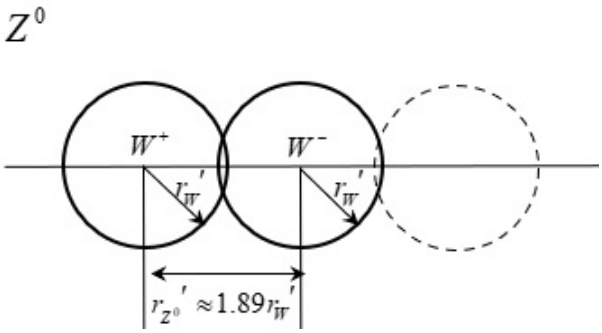



Figure 1: **Schematic of the $Z^0$ boson as the lowest $W^+W^-$ composite level.** The constituents are shown in a near-contact, strong-overlap configuration representing the most tightly bound level of the model. With the refined benchmark values, $r'_{Z^0} \simeq 1.89 r'_W$. The $S = 1$ assignment follows separately from the coupled-spin structure discussed in the text.

The refined binding model combines electromagnetic attraction with the short-distance weak Yukawa contribution,

$$U_{\text{binding}}^{(n)} = -\frac{(\alpha_{\text{em}} + \alpha_W)\hbar c}{r'_n} + \alpha_W m_W c^2. \tag{44}$$

Solving for the characteristic distance gives

$$r'_n = \frac{(\alpha_{\text{em}} + \alpha_W)\hbar c}{|U_{\text{binding}}^{(n)}| + \alpha_W m_W c^2}. \tag{45}$$

For the two observed states,

$$r'_{Z^0} \simeq 1.122 \times 10^{-19}\,\text{m}, \qquad r'_{X_1} \simeq 2.120 \times 10^{-19}\,\text{m}, \tag{46}$$

and therefore

$$\frac{r'_{X_1}}{r'_{Z^0}} \simeq 1.889. \tag{47}$$

The short-distance weak correction thus preserves the same near-two hierarchy found in the electrostatic approximation.

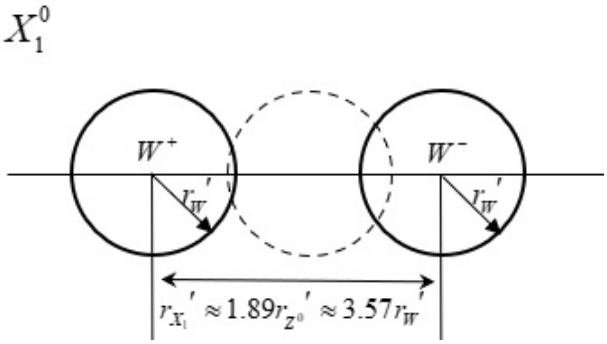



Figure 2: **Schematic of $X_1^0(125)$ as the next neutral $W^+W^-$ composite level.** The larger constituent-separation scale satisfies $r'_{X_1} \simeq 1.89 r'_{Z^0} \simeq 3.57 r'_W$. The reduced magnitude of the binding energy raises the total mass relative to the $Z^0$ level.

The spin structure is obtained by coupling two spin-1 constituents:

$$1 \otimes 1 = 0 \oplus 1 \oplus 2. \tag{48}$$

For the lowest orbital sector $L = 0$, one has $J = S$. The observed spins can then be accommodated by the model assignments

$$Z^0 : \quad S = 1, \quad L = 0, \quad J = 1, \tag{49}$$

and

$$X_1^0(125) : \quad S = 0, \quad L = 0, \quad J = 0 \tag{50}$$

[15,26,34]. The angular-momentum algebra permits these two channels, while their energetic ordering is determined by the full effective $W^+W^-$ interaction, including radial and spin-dependent contributions.

The resulting mass organization has a unified structure. Quark mass parameters are mapped to electromagnetic and effective strong-sector self-energy scales. The charged $W^\pm$ mass is mapped to electromagnetic and effective weak source energies. The neutral $Z^0$ and $X_1^0(125)$ masses are organized by the physical constituent masses together with the negative internal energies of two levels in a common $W^+W^-$ system [26].

The composite hypothesis predicts additional neutral levels above the first two observed assignments. Their masses, widths, and quantum numbers provide direct experimental tests of the $W^+W^-$ spectroscopic interpretation [26].

### 2.4 Effective Binding Dynamics of the Neutral $W^+W^-$ Sector

The mass relations obtained in Subsection 2.3 provide the first spectral constraints on the neutral $W^+W^-$ sector. At the present phenomenological level, the corresponding mass defects are identified primarily with the effective binding potential evaluated at the characteristic constituent separation,

$$U_{\text{binding}}^{(a)} \approx V_{\text{eff}}(r_n), \qquad a \in \{Z, X_1, X_2, \ldots\}. \tag{51}$$

This is a first static estimate of the binding-energy structure rather than a complete relativistic two-body calculation. Relative kinetic, retardation, radiative, and other dynamical corrections are not separated individually at this stage. Their net effects may be absorbed into the effective interaction terms and can be resolved in a later microscopic treatment.

A minimal static effective-energy description of the neutral $W^+W^-$ sector may be written as

$$E_{\rm eff}(r,S,L) = 2m_W c^2 + V_{\rm em}(r) + V^{\rm eff}_{\rm weak}(r,S,L) + \cdots , \tag{52}$$

$$\begin{aligned} V^{\rm eff}_{\rm weak}(r,S,L) = {} & V_{\rm W,C}(r) + V_{\rm SS}(r)\,\mathbf{s}_1\cdot\mathbf{s}_2 \\ & + V_{\rm T}(r)S_{12} + V_{\rm LS}(r)\,\mathbf{L}\cdot\mathbf{S} + \cdots . \end{aligned} \tag{53}$$

Thus, in the present static description,

$$V_{\rm eff}(r,S,L) \equiv V_{\rm em}(r) + V^{\rm eff}_{\rm weak}(r,S,L) + \cdots .$$

Here $r$ is the characteristic separation between the $W^+$ and $W^-$ constituents. The dimensionless constituent-spin operators are defined by

$$\mathbf{s}_i \equiv \frac{\mathbf{S}_i}{\hbar}, \tag{54}$$

and the tensor operator is

$$S_{12} = 3\,(\mathbf{s}_1\cdot\hat{\mathbf{r}})\,(\mathbf{s}_2\cdot\hat{\mathbf{r}}) - \mathbf{s}_1\cdot\mathbf{s}_2. \tag{55}$$

The observed masses impose the static spectral conditions

$$E_{\rm eff}(r_Z, S=1, L=0) = M_Z c^2, \tag{56}$$

and

$$E_{\rm eff}(r_X, S=0, L=0) = M_{X_1} c^2. \tag{57}$$

Accordingly, the effective interaction terms must reproduce both the measured mass defects and the model assignments consistent with the observed total spins of the first two neutral levels [15, 26].

The leading electromagnetic contribution is the attractive interaction between the oppositely charged constituents,

$$V_{\rm em}(r) \simeq -\frac{\alpha_{\rm em}\hbar c}{r}. \tag{58}$$

The quantity $V^{\rm eff}_{\rm weak}(r,S,L)$ collectively represents the effective weak-sector interaction adopted in the present phenomenological description. It incorporates the finite-range weak contribution together with short-distance non-Abelian and other weak-interaction effects relevant to the neutral $W^+W^-$ binding dynamics. Its explicit radial form and coupling structure are to be derived by matching to the underlying gauge-complete Higgs-free electroweak action.

The spin–spin term $V_{\rm SS}(r)\mathbf{s}_1\cdot\mathbf{s}_2$ organizes the splitting among the allowed total-spin channels. The tensor interaction $V_{\rm T}(r)S_{12}$ couples the constituent spins to their relative direction and can generate partial-wave mixing. The spin–orbit interaction $V_{\rm LS}(r)\mathbf{L}\cdot\mathbf{S}$ becomes relevant for orbital excitations with $L \neq 0$.

Finite constituent structure may be incorporated through form factors or through the effective radial dependence of $V^{\rm eff}_{\rm weak}(r,S,L)$. This potential-based organization follows the general spectroscopic practice of separating central and spin-dependent interactions, although the specific $W^+W^-$ weak kernel must be derived independently [35–37].

Using the spin decomposition introduced in Subsection 2.3, the spin–spin operator satisfies

$$\mathbf{s}_1 \cdot \mathbf{s}_2 = \frac{1}{2}\left[S(S+1) - s_1(s_1+1) - s_2(s_2+1)\right]. \tag{59}$$

For $s_1 = s_2 = 1$, this gives

$$\mathbf{s}_1 \cdot \mathbf{s}_2 = \begin{cases} -2, & S = 0, \\ -1, & S = 1, \\ +1, & S = 2. \end{cases} \tag{60}$$

This spin algebra provides the scalar, vector, and tensor channels available to the neutral $W^+W^-$ system [34].

In the spectroscopic assignment adopted here, the observed $Z^0$ is the lowest assigned neutral vector level,

$$Z^0 : \qquad S = 1, \qquad L = 0, \qquad J = 1, \tag{61}$$

whereas $X_1^0(125)$ is assigned to the observed scalar level,

$$X_1^0(125) : \qquad S = 0, \qquad L = 0, \qquad J = 0. \tag{62}$$

The full effective interaction, including its radial and spin-dependent contributions, must therefore be consistent with the ordering of the $n_r = 0$, $S = 1$ $Z^0$ level below the $n_r = 1$, $S = 0$ $X_1^0(125)$ level.

The remaining $S = 2$ channel provides one possible quantum-number assignment for an additional neutral state. Radial excitation, orbital excitation, and mixed configurations provide further possibilities. The spin algebra permits these higher channels, while their masses and ordering must be determined by the detailed effective interaction and experiment.

Using the binding energies obtained in Subsection 2.3, the static approximation of Eq. (39) gives the potential-depth conditions

$$V_{\text{eff}}(r_Z, S = 1, L = 0) \simeq -69.550\,\text{GeV}, \tag{63}$$

and

$$V_{\text{eff}}(r_X, S = 0, L = 0) \simeq -35.538\,\text{GeV}. \tag{64}$$

Thus, the measured $Z^0$ and $X_1^0(125)$ masses act as two quantitative matching conditions on a common neutral-sector binding potential [26].

The additional radial excitation and its corresponding mass interval are developed in Subsection 2.5.

The effective static description therefore organizes the $Z^0$, $X_1^0(125)$, and candidate $X_2^0$ levels through a common binding potential with different characteristic separations and spin configurations. The first two observed masses fix two potential-depth conditions, while the additional $X_2^0$ interval supplies a direct falsifiable target. A later action-derived microscopic treatment can determine the individual electromagnetic, weak, spin-dependent, kinetic, and relativistic contributions to this common neutral $W^+W^-$ spectrum.

A complementary timing consistency check, comparing these characteristic binding-response scales with the finite isolated-$W$ lifetime, is given in Appendix C.

## 2.5 A Radial-Excitation Prediction of an Additional Neutral Resonance Near 135.4 GeV

A physical framework gains direct empirical content when its interpretation of known states leads to experimentally testable predictions. In the present Higgs-free composite picture, the observed $Z^0$ boson and the 125 GeV scalar state $X_1^0(125)$ are assigned to the first two radially ordered levels of a common neutral $W^+W^-$ system [26]. The same structure then implies an additional neutral excitation above $X_1^0(125)$.

The systematic increase in the characteristic constituent separation,

$$r'_{Z^0} < r'_{X_1} < r'_{X_2}, \tag{65}$$

provides the geometric basis for interpreting these states as a radial excitation sequence. We therefore assign

$$Z^0: \quad n_r = 0, \qquad X_1^0(125): \quad n_r = 1, \qquad X_2^0: \quad n_r = 2, \tag{66}$$

where $n_r$ denotes the radial excitation index.

At the present phenomenological level, this radial assignment is inferred from the increasing constituent-separation scale rather than from an explicit solution for the radial wavefunction nodes. A microscopic solution of the effective $W^+W^-$ binding equation must determine the corresponding node structure and provide the final quantum-mechanical validation of this classification.

We denote the next neutral-state candidate by $X_2^0$. This notation leaves its total angular momentum open and avoids identifying the state prematurely as a specifically vector $Z$-type resonance.

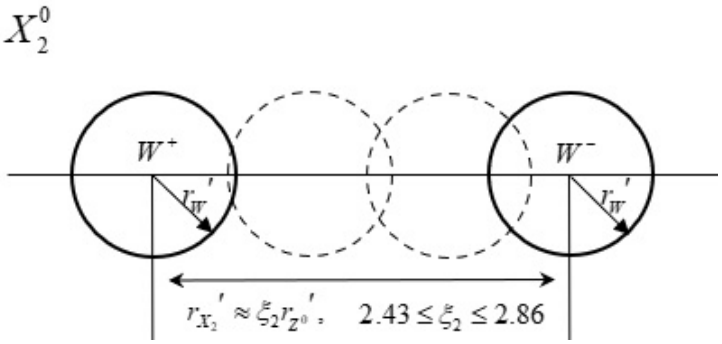



Figure 3: **Proposed neutral electroweak spectroscopy.** The benchmark $X_2^0$ resonance target near 135.4 GeV extends the sequence $Z^0 \to X_1^0(125) \to X_2^0$. The increasing constituent-separation scale is interpreted as the radial excitation sequence $n_r = 0 \to 1 \to 2$, while the spin configuration may also change between successive levels.

The refined characteristic distances of the first two levels satisfy approximately

$$r'_{Z^0} \simeq 1.89 r'_W, \qquad r'_{X_1} \simeq 3.57 r'_W, \tag{67}$$

and hence

$$\frac{r'_{X_1}}{r'_{Z^0}} \simeq 1.89. \tag{68}$$

The next radial scale is parameterized by the geometric extrapolation

$$r'_{X_2} = \xi_2 r'_{Z^0}, \qquad 2.43 \lesssim \xi_2 \lesssim 2.86. \tag{69}$$

This interval represents the second radial-excitation range adopted in the preceding composite analysis [26].

Using the same refined effective binding potential employed for the lower neutral levels,

$$U_{\mathrm{binding}}^{(X_2)}(r'_{X_2}) \simeq -\frac{(\alpha_{\mathrm{em}} + \alpha_W)\hbar c}{r'_{X_2}} + \alpha_W m_W c^2, \tag{70}$$

the mass of the additional state is written as

$$M_{X_2}c^2 = 2m_W c^2 + U_{\mathrm{binding}}^{(X_2)}(r'_{X_2}). \tag{71}$$

Applying the radial interval in Eq. (69) gives

$$133.7\,\mathrm{GeV} \lesssim M_{X_2}c^2 \lesssim 138.2\,\mathrm{GeV}, \tag{72}$$

with the representative benchmark

$$M_{X_2}c^2 \simeq 135.4\,\mathrm{GeV}. \tag{73}$$

The mass interval follows from the adopted radial-distance extrapolation, whereas 135.4 GeV is a representative benchmark within that interval rather than a uniquely calculated eigenvalue [26].

The constituent-spin decomposition remains that introduced in Subsection 2.3. The first two observed assignments are

$$Z^0: \qquad n_r = 0, \quad S = 1, \quad L = 0, \quad J = 1, \tag{74}$$

and

$$X_1^0(125): \qquad n_r = 1, \quad S = 0, \quad L = 0, \quad J = 0. \tag{75}$$

For the predicted second radial excitation,

$$X_2^0: \qquad n_r = 2, \tag{76}$$

the total-spin assignment remains to be determined.

A possible low-orbital assignment is the tensor channel

$$S = 2, \qquad L = 0, \qquad J = 2. \tag{77}$$

Vector or scalar radial configurations and states involving nonzero orbital angular momentum also remain possible. The mass extrapolation therefore fixes the proposed radial level but does not uniquely determine its total angular momentum.

The primary falsifiable prediction of this radial extrapolation is an additional neutral resonance in the 133.7–138.2 GeV interval. Observation of a state in this region with production, decay, width, and angular properties compatible with the $W^+W^-$ spectroscopic assignments would provide direct support for the proposed composite sequence [26].

A resonance at the predicted mass alone would not uniquely establish a $W^+W^-$ composite origin. The relevant experimental observables include

$$\sigma(pp \to X_2^0), \qquad \Gamma_{X_2^0}, \qquad \mathrm{BR}(X_2^0 \to D), \qquad J^P_{X_2^0}, \tag{78}$$

where $D$ denotes accessible channels such as $\gamma\gamma$, $Z\gamma$, $ZZ^*$, $WW^*$, and fermion pairs.

Null searches constrain the framework through upper limits on

$$\sigma(pp \to X_2^0) \times \mathrm{BR}(X_2^0 \to D). \tag{79}$$

A quantitative exclusion test therefore requires predictions for the production rates, total width, branching fractions, and angular distributions of the proposed state.

The resulting spectroscopic sequence can be summarized as

$$Z^0(n_r = 0, J = 1) \longrightarrow X_1^0(125)(n_r = 1, J = 0) \longrightarrow X_2^0(n_r = 2, J \text{ to be determined}). \tag{80}$$

It defines a radial electroweak spectroscopy program in which the increasing constituent separation, decreasing binding magnitude, and changing spin configuration jointly organize the neutral $W^+W^-$ spectrum. Dedicated searches at the LHC and future colliders can therefore test both the predicted mass interval and the correlated radial and spin structure of the Higgs-free composite framework.

## 2.6 Mass-Eigenstate Effective-Coupling Parameterization of $X_1^0(125)$

The 125 GeV resonance discovered by the ATLAS and CMS Collaborations has measured properties broadly consistent with the Standard Model Higgs benchmark [9, 10, 15]. In the present framework, the same observed state is interpreted as the neutral scalar $W^+W^-$ composite level $X_1^0(125)$ [26].

To compare this interpretation with collider observables, we introduce a phenomenological broken-phase effective-coupling parameterization. It describes the interactions of the observed mass eigenstate without assuming that the state is the quantum excitation of a fundamental Higgs condensate.

Kinematic accessibility determines which final states are open, whereas the observed production and decay pattern also constrains the relative coupling strengths and Lorentz structures. The composite interpretation must therefore reproduce the correlated signal strengths and differential distributions across the measured production and decay channels [15, 38].

We denote the composite scalar field by

$$X \equiv X_1^0(125). \tag{81}$$

At the broken-phase amplitude level, its leading CP-even interactions may be parameterized as

$$\begin{aligned}
\mathcal{L}_{\mathrm{eff}}^{X} = {} & g_{XWW}\, X W_\mu^+ W^{-\mu} + \frac{1}{2} g_{XZZ}\, X Z_\mu Z^\mu - \sum_f y_{Xf}\, X \bar{f} f \\
& + \frac{1}{2} c_{WW}\, X W_{\mu\nu}^+ W^{-\mu\nu} + \frac{1}{4} c_{ZZ}\, X Z_{\mu\nu} Z^{\mu\nu} \\
& + \frac{1}{2} c_{Z\gamma}\, X Z_{\mu\nu} F^{\mu\nu} + \frac{1}{4} c_{\gamma\gamma}\, X F_{\mu\nu} F^{\mu\nu} \\
& + \frac{1}{4} c_{gg}\, X G_{\mu\nu}^a G^{a\mu\nu} + \cdots .
\end{aligned} \tag{82}$$

The coefficients $g_{XWW}$ and $g_{XZZ}$ have mass dimension one, $y_{Xf}$ is dimensionless, and the field-strength coefficients $c_i$ have mass dimension minus one. CP-odd operators containing dual field strengths are omitted in accordance with the CP-even scalar assignment.

The terms proportional to $g_{XWW}$, $g_{XZZ}$, and $y_{Xf}$ describe the leading nonderivative interactions. The coefficients $c_{WW}$, $c_{ZZ}$, $c_{Z\gamma}$, $c_{\gamma\gamma}$, and $c_{gg}$ describe additional momentum-dependent

and loop-like structures relevant to vector boson processes, diphoton and $Z\gamma$ decays, and gluon-fusion production [38, 39].

Equation (82) is a broken-phase mass-eigenstate parameterization rather than the final gauge-complete action. The underlying Higgs-free electroweak construction must derive its coefficient relations, momentum dependence, and the corresponding Ward and Slavnov–Taylor identities.

With the normalization used in Eq. (82), the corresponding tree-level Standard Model benchmark values are

$$g_{hWW}^{\mathrm{SM}} = \frac{2m_W^2}{v}, \qquad g_{hZZ}^{\mathrm{SM}} = \frac{2M_Z^2}{v}, \qquad y_{hf}^{\mathrm{SM}} = \frac{m_f}{v}, \tag{83}$$

where $v$ denotes the Standard Model Higgs vacuum expectation value [14, 15]. These equations are used only as Standard Model comparison values. The composite coefficients in Eq. (82) originate from the $W^+W^-$ internal dynamics rather than from fundamental Yukawa interactions or a scalar condensate.

For the nonderivative interactions, coupling modifiers may be defined by

$$\kappa_W^X \equiv \frac{g_{XWW}}{g_{hWW}^{\mathrm{SM}}}, \qquad \kappa_Z^X \equiv \frac{g_{XZZ}}{g_{hZZ}^{\mathrm{SM}}}, \qquad \kappa_f^X \equiv \frac{y_{Xf}}{y_{hf}^{\mathrm{SM}}}. \tag{84}$$

Values near unity indicate numerical agreement with the corresponding Standard Model benchmark, but they do not by themselves determine the microscopic origin of the state. The field-strength operators and their kinematic dependence must be included when comparing differential distributions or high-energy vector-boson processes.

Composite interactions may acquire form factors. We write schematically

$$g_i^{\mathrm{eff}} \longrightarrow g_i^{\mathrm{eff}} \mathcal{F}_i\left(q^2, p_1^2, p_2^2\right), \tag{85}$$

with a channel-dependent near-pole reference normalization

$$\mathcal{F}_i\left(M_X^2, \bar{p}_{1,i}^{\,2}, \bar{p}_{2,i}^{\,2}\right) = 1. \tag{86}$$

Here $\bar{p}_{1,i}^{\,2}$ and $\bar{p}_{2,i}^{\,2}$ denote the reference virtualities chosen for channel $i$. The constant-coupling approximation describes the near-pole region, whereas deviations in high-energy differential observables probe momentum dependence associated with the internal structure.

For a production mode $P$ and decay channel $D$, the collider signal strength is defined as

$$\mu_{P,D} \equiv \frac{\sigma_P(pp \to X)\,\mathrm{BR}(X \to D)}{[\sigma_P(pp \to h)\,\mathrm{BR}(h \to D)]_{\mathrm{SM}}}. \tag{87}$$

In the narrow-width approximation and for comparable experimental acceptances,

$$\mu_{P,D}^{\mathrm{comp}} = \frac{\sigma_P^{\mathrm{comp}}}{\sigma_P^{\mathrm{SM}}} \frac{\Gamma_D^{\mathrm{comp}}}{\Gamma_D^{\mathrm{SM}}} \frac{\Gamma_{\mathrm{tot}}^{\mathrm{SM}}}{\Gamma_{\mathrm{tot}}^{\mathrm{comp}}}. \tag{88}$$

When the composite Lorentz structures modify event kinematics, the acceptance and reconstruction efficiency must also be included,

$$\mu_{P,D}^{\mathrm{obs}} = \frac{\left[\sigma_P\,\mathrm{BR}_D\,\mathcal{A}_{P,D}\epsilon_{P,D}\right]_{\mathrm{comp}}}{\left[\sigma_P\,\mathrm{BR}_D\,\mathcal{A}_{P,D}\epsilon_{P,D}\right]_{\mathrm{SM}}}. \tag{89}$$

Approximately Standard-Model-like signal strengths indicate that the composite production and decay rates numerically reproduce the measured benchmarks within the quoted experimental uncertainties [15, 38].

A phenomenological fit may initially treat the coefficients in Eq. (82) as independent. A microscopic $W^+W^-$ composite theory must subsequently derive correlations among them from the common constituent wavefunction and transition kernels. Schematically,

$$g_i^{\text{eff}} \sim \left\langle D_i \left| \widehat{\mathcal{O}}_i \right| \Psi^{(X)}_{W^+W^-} \right\rangle, \tag{90}$$

where $\Psi^{(X)}_{W^+W^-}$ is the scalar composite wavefunction and $\widehat{\mathcal{O}}_i$ is the corresponding transition operator.

Precision measurements of vector-boson scattering, differential production, loop-sensitive channels, fermionic couplings, and searches for the predicted neutral resonance therefore provide complementary tests of the Higgs-free composite interpretation.

## 3 Physical Organization of the Higgs-Free Electroweak Model

The Higgs sector occupies a central position in the Standard Model. Its gauge-covariant scalar dynamics generates the $W^\pm$ and $Z^0$ mass terms after the scalar field acquires a nonzero vacuum expectation value and supplies the corresponding longitudinal degrees of freedom. Through Yukawa interactions, the same scalar sector parameterizes the masses of quarks and charged leptons [14, 15].

The discovery of a neutral scalar resonance near 125 GeV by the ATLAS and CMS Collaborations established the Standard Model Higgs interpretation as the experimentally preferred and conventionally adopted description of the observed state [9, 10, 15]. In that interpretation, the resonance is the quantum excitation of the scalar field whose vacuum expectation value sets the electroweak mass scale.

The empirical success of this framework is substantial. The minimal Standard Model nevertheless leaves several central quantities as phenomenological inputs rather than deriving them from a deeper dynamical sector. The sign and magnitude of the Higgs quadratic term, the electroweak scale

$$v \simeq 246\,\text{GeV}, \tag{91}$$

and the hierarchy of fermion Yukawa couplings enter through experimentally determined parameters. The minimal renormalizable Standard Model leaves neutrinos massless and does not provide a dynamical explanation or symmetry protection for the large separation between the electroweak scale and much higher fundamental scales. Its nonzero vacuum structure also enters the broader gravitational vacuum-energy problem [14, 15, 21]. The same 125 GeV resonance is interpreted in the present framework through the $W^+W^-$ binding-energy model [26].

These open questions motivate the Higgs-free construction developed here. The present framework assigns the physical origin of particle masses to self-energy, internal energy, binding energy, and composite dynamics. Separate structural layers then provide the massive-vector gauge representation, high-energy longitudinal control, and trans-Planckian ultraviolet suppression.

### 3.1 Charge Self-Energy as the Primary Mass Origin in the Present Framework

A finite spatial distribution of charge carries a field-configuration self-energy. In classical electrodynamics, the field-energy representation and the charge–potential representation satisfy

$$U_{\mathrm{em}} = \frac{\epsilon_0}{2}\int d^3x\,\mathbf{E}^2 = \frac{1}{2}\int d^3x\,\rho\phi. \tag{92}$$

These expressions describe the same physical electromagnetic self-energy and must not be added as independent contributions [24, 25].

For an interaction that is approximately dominated by a $1/R$ structure over the relevant range, the self-energy of a finite configuration may be written schematically as

$$U_{\mathrm{self}}^{(a)}(R) = \eta_a\beta_a\frac{C_aQ_a^2}{R}, \qquad \eta_a = \pm 1, \tag{93}$$

where $a$ labels the interaction sector, $Q_a$ is the corresponding effective charge, $C_a$ is its interaction coefficient, $\beta_a$ is a structure factor determined by the internal distribution, and $\eta_a$ specifies the sign of the contribution.

The electromagnetic and Newtonian gravitational examples are

$$U_{\mathrm{em}} = +\beta_{\mathrm{em}}\frac{k_eQ_e^2}{R}, \qquad U_{\mathrm{grav}} = -\beta_{\mathrm{g}}\frac{GM^2}{R}. \tag{94}$$

Equation (93) is a schematic finite-size relation rather than a universal expression for every interaction. The weak and strong sectors may require more general radial energy functions,

$$U_{\mathrm{weak}} = U_{\mathrm{weak}}(Q_w,R), \qquad U_{\mathrm{strong}} = U_{\mathrm{strong}}(Q_s,R). \tag{95}$$

The present framework applies this energy accounting to localized particle excitations. Its general rest-energy budget takes the form

$$mc^2 = U_{\mathrm{SE}} + T_{\mathrm{int}} + U_{\mathrm{bind}} + \cdots, \tag{96}$$

with

$$U_{\mathrm{SE}} = U_{\mathrm{em}} + U_{\mathrm{weak}} + U_{\mathrm{strong}} + U_{\mathrm{grav}}. \tag{97}$$

Here $U_{\mathrm{grav}}$ denotes the total gravitational self-energy contribution, reducing to the Newtonian term in the low-compactness limit.

Each term represents a physically distinct contribution. Their definitions must prevent repeated counting of the same field or interaction energy.

For the charged weak boson, the model assigns the dominant rest-energy scale to electromagnetic and weak-sector self-energy,

$$m_Wc^2 \simeq U_{\mathrm{em}}^{(W)} + U_{\mathrm{weak}}^{(W)} + \cdots. \tag{98}$$

The weak contribution is represented by the effective finite-size functional

$$U_{\mathrm{weak}}^{(W)} = U_{\mathrm{weak}}(Q_w,R_W). \tag{99}$$

Equation (98) defines the principal mass-origin hypothesis of the framework.

This hypothesis reverses the conventional order of the electroweak mass problem. The Standard Model begins with a massless electroweak gauge sector and generates the $W^{\pm}$ and $Z^0$ masses through the Higgs vacuum. The present framework first assigns a finite self-energy

mass scale to the charged weak excitation and then constructs a gauge-compatible representation of the resulting massive-vector sector.

A Stückelberg-type compensating structure supplies this massive-vector gauge representation. It introduces a gauge redundancy compatible with a nonzero vector mass after the physical mass scale has been assigned to self-energy. The Stückelberg layer therefore provides the gauge-structural starting point rather than an automatic proof of the full interacting completion.

The logical distinction can be summarized as follows.

Table 1: Logical distinction between the Standard Model Higgs construction and the proposed self-energy framework.

| Framework | Physical origin assigned to the mass scale | Gauge-structure realization |
|---|---|---|
| Standard Model Higgs sector | A scalar-doublet vacuum expectation value generates the weak-boson mass terms, while Yukawa couplings parameterize charged-fermion masses | The gauge-invariant scalar and gauge action generates the massive-vector structure and supplies the longitudinal degrees of freedom |
| Proposed self-energy framework | Finite self-energy, internal energy, and composite binding generate the physical rest-energy scale | A Stückelberg-type compensating structure supplies the massive-vector gauge representation, while the non-Abelian and high-energy completion is developed in separate structural layers |

The framework therefore separates the physical origin of mass from the gauge representation of a massive vector field:

$$\text{physical mass origin} \quad \longrightarrow \quad \text{self-energy and composite dynamics,} \tag{100}$$

whereas

$$\text{massive-vector gauge representation} \quad \longrightarrow \quad \text{Stückelberg-type compensating structure.} \tag{101}$$

### 3.2 Vacuum Energy, Spacetime Curvature, and the Higgs Vacuum

The vacuum structure of the conventional Higgs sector provides a second central motivation. Using natural units, $\hbar = c = 1$, the renormalizable scalar potential may be written as

$$V(\Phi) = V_0 - \mu^2 \Phi^\dagger \Phi + \lambda \left(\Phi^\dagger \Phi\right)^2, \tag{102}$$

where $V_0$ is an additive constant. With

$$\Phi = \frac{1}{\sqrt{2}} \begin{pmatrix} 0 \\ v + h \end{pmatrix}, \tag{103}$$

the broken minimum satisfies

$$v^2 = \frac{\mu^2}{\lambda}, \qquad m_h^2 = 2\lambda v^2 = 2\mu^2. \tag{104}$$

The potential values at the symmetric and broken configurations are

$$V(0) = V_0, \qquad V(v) = V_0 - \frac{\mu^4}{4\lambda}. \tag{105}$$

In nongravitational quantum field theory, the constant $V_0$ shifts the absolute value of the potential without changing its stationary points, the vacuum expectation value, or the conventional particle-mass relations. The local formulas

$$m_W = \frac{gv}{2}, \qquad M_Z = \frac{\sqrt{g^2 + g'^2}}{2} v, \qquad m_f = \frac{y_f v}{\sqrt{2}} \tag{106}$$

therefore remain unchanged under an additive shift of the potential when the spacetime background is held fixed.

The additive shift does not remove the energy difference between the symmetric and broken phases. If the conventional choice

$$V_0 = 0 \tag{107}$$

sets the symmetric configuration to zero, then

$$V(0) = 0, \qquad V(v) = -\frac{\mu^4}{4\lambda} < 0. \tag{108}$$

Alternatively, setting the broken vacuum to zero requires

$$V_0 = \frac{\mu^4}{4\lambda}, \tag{109}$$

which gives

$$V(v) = 0, \qquad V(0) = \frac{\mu^4}{4\lambda} > 0. \tag{110}$$

A single additive constant cannot set both phases to zero. The phase difference remains

$$\Delta V_{\mathrm{EW}} \equiv V(v) - V(0) = -\frac{\mu^4}{4\lambda} = -\frac{m_h^2 v^2}{8}. \tag{111}$$

In a gravitational theory, a constant vacuum-energy contribution enters the effective cosmological constant. A vacuum contribution satisfies

$$T^{\mathrm{vac}}_{\mu\nu} = -V_{\mathrm{vac}} g_{\mu\nu}. \tag{112}$$

The Einstein equation may therefore be written as

$$G_{\mu\nu} + \Lambda_{\mathrm{bare}} g_{\mu\nu} = 8\pi G \left( T^{\mathrm{matter}}_{\mu\nu} - V_{\mathrm{vac}} g_{\mu\nu} \right), \tag{113}$$

or equivalently

$$G_{\mu\nu} + \Lambda_{\mathrm{eff}} g_{\mu\nu} = 8\pi G T^{\mathrm{matter}}_{\mu\nu}, \qquad \Lambda_{\mathrm{eff}} = \Lambda_{\mathrm{bare}} + 8\pi G V_{\mathrm{vac}}. \tag{114}$$

For fixed $\Lambda_{\mathrm{bare}}$, changing $V_0$ changes $\Lambda_{\mathrm{eff}}$ and hence the spacetime solution. Introducing an opposite shift in $\Lambda_{\mathrm{bare}}$ merely imposes a cancellation by hand; it does not explain why physically distinct vacuum contributions should cancel to the extraordinary precision required by the observed late-time vacuum energy. At the electroweak scale, the required adjustment is of order $10^{-55}$. Its persistence in the presence of radiative corrections and vacuum transitions is itself

the central fine-tuning problem, for which the minimal Higgs sector supplies no dynamical explanation [21].

The altered spacetime can also feed back into the scalar dynamics. For sufficiently small curvature and minimal coupling, the local electroweak mass relations remain approximately unchanged. A general curved-spacetime effective action, however, permits the nonminimal interaction [40]

$$S_{\Phi R} = -\int d^4x\,\sqrt{-g}\,\xi R\Phi^\dagger\Phi. \tag{115}$$

With this sign convention, the curvature-dependent effective potential contains

$$V_{\rm eff}(\Phi,R) = V(\Phi) + \xi R\Phi^\dagger\Phi + \cdots, \tag{116}$$

and its nonzero minimum satisfies schematically

$$v^2(R) = \frac{\mu^2 - \xi R}{\lambda}. \tag{117}$$

Spacetime curvature can therefore modify the scalar vacuum structure, especially in high-curvature backgrounds or when the nonminimal coupling is significant.

The gravitational cancellation of the Higgs vacuum energy is consequently not entirely external to Higgs dynamics. The cancellation determines the effective curvature background, and the curvature can influence the scalar minimum. The central tension is not that an additive constant algebraically destroys the Higgs mass mechanism. The tension is that the same electroweak vacuum structure produces a large change in the gravitational source, while the observed late-time spacetime requires an extremely small renormalized vacuum energy.

For the measured electroweak parameters, the magnitude of the tree-level electroweak vacuum-energy difference is approximately

$$|\Delta V_{\rm EW}| = \frac{m_h^2 v^2}{8} \sim 10^8\,{\rm GeV}^4, \tag{118}$$

whereas the observed late-time dark-energy density is of order

$$\rho_{\rm DE}^{\rm obs} \sim 10^{-47}\,{\rm GeV}^4. \tag{119}$$

The two scales differ by approximately fifty-five orders of magnitude. A fine-tuning at the level of $10^{55}$ constitutes a severe problem. A single constant can cancel the tree-level contribution at one chosen stage, but the theory must explain how the required cancellation is maintained or replaced by a physical mechanism in the presence of radiative corrections, the electroweak transition, the QCD transition, and other vacuum contributions [21].

Maintaining both the electroweak vacuum expectation value and the observed near-flat gravitational background therefore requires an explanation of the $10^{55}$-level cancellation or an alternative physical mechanism that removes, compensates, or gravitationally decouples the large vacuum contribution. The minimal Higgs sector does not provide such an explanation.

The present framework adopts a different electroweak mass architecture. It does not assign weak-boson and fermion masses to a fundamental scalar vacuum expectation value. Instead, it assigns charged-sector rest energies to self-energy and organizes the neutral electroweak sector as a composite $W^+W^-$ family,

$$W^+W^- \quad\longrightarrow\quad Z^0,\, X_1^0(125),\, X_2^0, \ldots. \tag{120}$$

The observed $Z^0$ and $X_1^0(125)$ states are assigned to the first two radially ordered neutral levels [26].

Removing a fundamental Higgs condensate from the electroweak mass mechanism eliminates that specific scalar-vacuum contribution from the mass-generation architecture.

The broader matter-only cosmology and total-GSE program identifies dark energy with matter-induced gravitational self-energy rather than with a fundamental dark energy field and presents an explicit dark energy density derived from total GSE [32, 33].

### 3.3 Reframing the Electroweak Mass Problem

The preceding arguments reorganize the electroweak mass problem. A finite localized charge distribution carries self-energy, whereas the minimal Higgs sector contains an empirically fixed scalar scale, an unexplained Yukawa hierarchy, and a Higgs-sector vacuum contribution whose reconciliation with the observed vacuum-energy scale requires a fine-tuning of approximately $10^{55}$ or an alternative physical mechanism.

The present framework separates the electroweak problem into distinct physical layers:

$$\begin{aligned}
\text{mass origin} &\longrightarrow \text{self-energy, internal energy, and composite binding,}\\
\text{massive-vector gauge structure} &\longrightarrow \text{Stückelberg-type compensating fields,}\\
\text{neutral spectroscopy} &\longrightarrow W^+W^- \text{ composite radial levels,}\\
\text{TeV-scale longitudinal behavior} &\longrightarrow \text{finite-formation principle,}\\
\text{trans-Planckian propagation} &\longrightarrow \text{KGC-dressed ultraviolet suppression.}
\end{aligned} \tag{121}$$

The charged weak sector begins with localized massive excitations whose rest energy arises from finite electromagnetic and weak-sector self-energy. The Stückelberg layer supplies the corresponding gauge-compatible massive-vector representation. The neutral sector arises from $W^+W^-$ composite dynamics, and the increasing constituent-center separation defines a radially ordered spectroscopic sequence.

The framework assigns the TeV-scale longitudinal problem to the proposed finite-formation principle. It assigns the trans-Planckian sector to KGC-dressed propagation, in which the equivalent momentum grows rapidly and suppresses ultraviolet propagation within the stated effective framework [30].

These layers define a first-stage replacement framework rather than a completed Higgs-free Standard Model. Their common non-Abelian realization constitutes a subsequent action-level stage, with its principal consistency conditions developed below.

The central physical proposal can be summarized as

$$\boxed{\begin{array}{c}\text{mass from self-energy and binding}\\ + \text{ gauge compatibility through compensating fields}\\ + \text{ neutral spectroscopy from composite dynamics}\end{array}} \tag{122}$$

together with independent mechanisms for high-energy longitudinal control and ultraviolet suppression. This organization replaces the fundamental Higgs vacuum as the common origin of electroweak masses and converts the mass problem into a set of directly testable dynamical questions.

# 4 Stückelberg Gauge Structure Without a Fundamental Higgs Condensate

In the conventional electroweak theory, the gauge-covariant Higgs sector simultaneously generates the weak-vector mass terms, supplies the corresponding longitudinal degrees of freedom, and fixes interaction structures that satisfy the gauge identities of the theory [14]. The present framework separates the physical origin assigned to the mass scale from the gauge representation of the resulting massive-vector sector.

The model assigns the physical origin of mass to self-energy, internal energy, binding energy, and composite dynamics rather than to a fundamental Higgs condensate. The charged weak bosons carry finite electromagnetic and weak-sector self-energy scales. The observed neutral states $Z^0$ and $X_1^0(125)$ are assigned to the first two radially ordered levels of an underlying $W^+W^-$ composite system [26].

The Stückelberg layer introduces compensating fields that organize the massive charged weak-vector sector in a gauge-compatible representation and parameterize its longitudinal degrees of freedom. The requirements for the corresponding non-Abelian completion are developed below.

## 4.1 Abelian Stückelberg Prototype

The Abelian theory provides the clearest realization of the Stückelberg construction [27, 28]. Adding the Proca mass term

$$\frac{1}{2}m_X^2 X_\mu X^\mu \tag{123}$$

directly to the Maxwell Lagrangian removes its $U(1)$ gauge invariance.

The Stückelberg formulation introduces a compensating scalar field $\sigma$ and replaces $X_\mu$ by the invariant combination

$$\mathcal{X}_\mu \equiv X_\mu - \frac{1}{m_X}\partial_\mu \sigma. \tag{124}$$

The corresponding Lagrangian is

$$\mathcal{L}_{\rm St} = -\frac{1}{4}X_{\mu\nu}X^{\mu\nu} + \frac{1}{2}m_X^2\left(X_\mu - \frac{1}{m_X}\partial_\mu\sigma\right)^2, \tag{125}$$

where

$$X_{\mu\nu} = \partial_\mu X_\nu - \partial_\nu X_\mu. \tag{126}$$

The transformations

$$X_\mu \to X_\mu + \partial_\mu \alpha(x), \qquad \sigma \to \sigma + m_X \alpha(x) \tag{127}$$

leave $\mathcal{X}_\mu$ and $\mathcal{L}_{\rm St}$ invariant. These transformations express a redundancy of the enlarged field description. They do not determine the numerical value or physical origin of $m_X$.

The free Abelian Stückelberg theory is dynamically equivalent to a massive spin-one field with three physical polarizations. The compensating field organizes the longitudinal sector in a form suitable for covariant gauge fixing and quantization [28].

### 4.2 Charged Weak-Sector Prototype and Non-Abelian Completion

The charged weak fields are defined by

$$W_\mu^\pm = \frac{1}{\sqrt{2}}\left(W_\mu^1 \mp i W_\mu^2\right). \tag{128}$$

At the linearized charged-sector level, an Abelianized Stückelberg parameterization may be written as

$$\mathcal{L}^W_{\mathrm{St,lin}} = \left(M_W^{\mathrm{SE}} W_\mu^+ - \partial_\mu \pi^+\right)\left(M_W^{\mathrm{SE}} W^{-\mu} - \partial^\mu \pi^-\right). \tag{129}$$

It is invariant under the linearized transformations

$$W_\mu^\pm \to W_\mu^\pm + \partial_\mu \alpha^\pm, \qquad \pi^\pm \to \pi^\pm + M_W^{\mathrm{SE}} \alpha^\pm. \tag{130}$$

The fields $\pi^\pm$ are not excitations of a fundamental Higgs doublet. They act as compensating longitudinal coordinates in the Stückelberg description and are mathematically analogous to would-be Goldstone variables in a nonlinear gauge realization.

Equation (**??**) is a charged-sector prototype rather than the complete $SU(2)_L \times U(1)_Y$ Stückelberg action. The fields $W_\mu^\pm$ are components of a non-Abelian gauge connection and do not transform as two independent Abelian gauge fields.

A standard non-Abelian Stückelberg-type template introduces a group-valued compensator

$$\Sigma(x) = \exp\left[\frac{i\pi^a(x)\tau^a}{f}\right], \tag{131}$$

with the transformation

$$\Sigma \to G_L \Sigma G_Y^\dagger, \qquad G_L \in SU(2)_L, \qquad G_Y = \exp\left[\frac{i\beta(x)\tau^3}{2}\right]. \tag{132}$$

Its electroweak covariant derivative is

$$D_\mu \Sigma = \partial_\mu \Sigma - i g W_\mu^a \frac{\tau^a}{2}\Sigma + i g' \Sigma \frac{\tau^3}{2} B_\mu, \tag{133}$$

and the leading invariant operator is

$$\mathcal{L}_\Sigma = \frac{f^2}{4}\,\mathrm{Tr}\left[(D_\mu \Sigma)^\dagger D^\mu \Sigma\right]. \tag{134}$$

This operator shows how a non-Abelian compensating structure can preserve the electroweak gauge transformations without introducing a fundamental radial Higgs excitation. It serves here as a covariance benchmark rather than as the final action of the present model.

In four dimensions, the non-Abelian Stückelberg realization is generally non-polynomial and not power-counting renormalizable. It therefore defines an effective field theory with a finite range of validity unless an additional ultraviolet completion modifies its high-energy behavior [28].

A further model-specific condition arises in the neutral sector. The standard operator in Eq. (134) produces both charged and neutral massive-vector combinations. The present framework, however, identifies the observed $Z^0$ resonance with a $W^+W^-$ composite pole. The final non-Abelian action must therefore avoid double counting between an elementary neutral Stückelberg mass eigenstate and the composite $Z^0$ state.

It must derive, within one common construction,

$$\text{a massless photon,} \qquad \text{the observed neutral currents,} \qquad \text{and the composite } Z^0 \text{ pole.} \tag{135}$$

### 4.3 Role and Scope of the Stückelberg Layer

The Stückelberg layer addresses a specific structural question: how an assigned massive-vector sector can be represented without inserting a bare mass term that explicitly violates the gauge redundancy of the enlarged field description.

In the present framework,

$$m_W c^2 \quad \longleftarrow \quad \text{electromagnetic and weak-sector self-energy,} \tag{136}$$

whereas

$$M_W^{\mathrm{SE}} \quad \longrightarrow \quad \text{mass parameter in the Stückelberg gauge representation,} \tag{137}$$

The separation can be summarized as

$$\text{physical mass origin} \quad \longrightarrow \quad \text{self-energy and composite dynamics,} \tag{138}$$

and

$$\text{massive-vector gauge representation} \quad \longrightarrow \quad \text{Stückelberg compensating fields.} \tag{139}$$

The Stückelberg representation preserves the gauge redundancy of the enlarged field description. The interacting non-Abelian weak sector then requires a high-energy completion that yields controlled longitudinal amplitudes and a consistent ultraviolet behavior over the intended energy range. Longitudinal-vector interactions can still produce amplitudes that grow with energy [28, 29].

The present framework assigns the TeV-scale longitudinal problem to the finite-formation principle developed in the next section.

The KGC construction provides the dressed scalar and gauge propagator structure, while the Dirac–Choi construction extends the same form-factor principle to a gauge-complete Abelian spinor sector with Ward–Takahashi control [30, 41]. Their non-Abelian extension requires BRST and Slavnov–Taylor control [42].

The trans-Planckian KGC mechanism and the TeV-scale finite-formation principle address different momentum regimes. Neither mechanism removes the need to construct the complete non-Abelian gauge action and to verify its physical amplitudes.

At the present stage, the Abelian Stückelberg theory and the linearized charged-sector expression provide a structural prototype. The complete Higgs-free electroweak gauge sector remains subject to the following conditions:

$$\begin{aligned}
&SU(2)_L \times U(1)_Y \text{ covariance,}\\
&\text{BRST and Slavnov–Taylor consistency,}\\
&\text{a massless photon and correct electromagnetic current,}\\
&\text{precision neutral-current matching,}\\
&\text{absence of double counting in the composite } Z^0 \text{ sector,}\\
&\text{controlled longitudinal vector-boson amplitudes.}
\end{aligned} \tag{140}$$

Satisfying these conditions will turn the Stückelberg prototype into the gauge-complete electroweak layer required by the self-energy and composite framework.

# 5 High-Energy Consistency and the TeV-Scale Longitudinal Issue

One standard consistency requirement of electroweak theory concerns the high-energy behavior of longitudinal weak-boson scattering. In a Higgsless electroweak effective theory, the leading longitudinal amplitudes grow schematically as $s/v^2$, and the corresponding partial waves reach the perturbative unitarity boundary in the TeV regime [14, 29].

For a representative angle-independent channel,

$$\mathcal{M}_0(s) \sim \frac{s}{v^2}, \tag{141}$$

and

$$a_0^{(0)}(s) \sim \frac{s}{16\pi v^2}. \tag{142}$$

The condition

$$\left|\mathrm{Re}\, a_0^{(0)}\right| \leq \frac{1}{2}. \tag{143}$$

gives the representative scale

$$\sqrt{s} \sim \sqrt{8\pi}\, v \simeq 1.23\,\mathrm{TeV}. \tag{144}$$

Separately, the naive-dimensional-analysis scale

$$\Lambda_\chi \sim 4\pi v \simeq 3.09\,\mathrm{TeV}, \qquad v \simeq 246\,\mathrm{GeV}, \tag{145}$$

marks the characteristic strong-coupling scale of the electroweak chiral effective theory [14,15, 29]. The partial-wave estimate and the NDA scale therefore identify complementary features of the same broad TeV-scale consistency problem.

The Stückelberg compensating structure organizes the massive weak-vector sector in a gauge-compatible representation and parameterizes its longitudinal degrees of freedom [27, 28].

The finite-formation principle governs the TeV-scale longitudinal dynamics, while the KGC sector governs trans-Planckian propagation. Their action-level embedding follows the gauge-completion structure discussed in Section 4.

The finite-formation and KGC sectors therefore address distinct high-energy regimes, while the Stückelberg layer provides the massive-vector gauge representation.

## 5.1 A Finite-Formation Suppression Ansatz Motivated by Time–Energy Uncertainty

The TeV-scale longitudinal issue and the trans-Planckian KGC regime occupy different energy domains. The present subsection introduces a finite-formation benchmark for the TeV-scale longitudinal response, while KGC dressing governs the much higher trans-Planckian propagation regime.

### 5.1.1 Amplitude-Level Finite-Formation Suppression

For a process characterized by an energy spread $\Delta E$, a characteristic evolution or formation time may be estimated as

$$\tau_E \sim \frac{\hbar}{2\Delta E}. \tag{146}$$

The present framework uses this relation as a physical timescale estimate for the development of a longitudinal weak-vector response [34].

Identifying the characteristic energy scale with $E \sim \Delta E$, the framework defines the causal formation scale

$$R_{\text{form}}(E) \equiv c\,\tau_E \sim \frac{\hbar c}{2E}. \tag{147}$$

This scale estimates the causal distance available for the coherent development of the longitudinal response.

The present framework identifies the effective self-energy-corrected weak radius $r'_W$ with the characteristic coherence length of the longitudinal weak-vector response [26]. A fully coherent response corresponds to

$$R_{\text{form}}(E) \gtrsim r'_W. \tag{148}$$

The regime

$$R_{\text{form}}(E) < r'_W \tag{149}$$

provides a shorter causal interval than the characteristic weak-response scale and motivates a reduced longitudinal formation factor.

The associated critical energy is

$$E_{\text{crit}} \equiv \frac{\hbar c}{2r'_W}. \tag{150}$$

For the representative radius

$$r'_W \simeq 5.93 \times 10^{-20}\,\text{m}, \tag{151}$$

one obtains

$$E_{\text{crit}} \simeq 1.66\,\text{TeV}. \tag{152}$$

This scale lies in the broad TeV region where Higgsless longitudinal amplitudes require additional dynamical control [14, 29].

A minimal phenomenological parameterization of the finite-formation response is

$$S_L(E) = \min\left(1, \frac{R_{\text{form}}(E)}{r'_W}\right) = \min\left(1, \frac{E_{\text{crit}}}{E}\right). \tag{153}$$

For amplitude calculations, the smooth benchmark

$$S_L(E) = \frac{1}{1 + E/E_{\text{crit}}} \tag{154}$$

provides the same low- and high-energy scaling without a discontinuous derivative.

In a gauge theory, the longitudinal polarization basis participates in gauge cancellations, Ward identities, and Slavnov–Taylor identities [14, 28]. Let

$$\mathcal{M}_0(s,t,u) \tag{155}$$

denote the complete Higgsless longitudinal amplitude before the finite-formation modification. The benchmark physical amplitude is written as

$$\mathcal{M}_{\text{HF}}(s,t,u) = \mathcal{M}_0(s,t,u)\,\mathcal{F}_L(s,t,u). \tag{156}$$

The factor $\mathcal{F}_L$ acts on the complete physical longitudinal amplitude or on a gauge-invariant coupled-channel eigenamplitude, rather than on selected diagrams. Its action-level embedding follows the common gauge structure discussed in Section 4. The KGC and Dirac–Choi constructions provide scalar, gauge, and Abelian spinor prototypes for this action-level organization [30, 41].

For a $2 \to 2$ process with four external longitudinal weak-vector responses, a symmetric benchmark assigns one smooth formation factor to each external longitudinal response. With

$$E_j \simeq \frac{\sqrt{s}}{2}, \qquad j = 1, \ldots, 4, \tag{157}$$

this gives

$$\mathcal{F}_L^{(4)}(s) = \prod_{j=1}^{4} S_L(E_j) \simeq \left(1 + \frac{\sqrt{s}}{2E_{\rm crit}}\right)^{-4}. \tag{158}$$

Equation (158) defines a phenomenological four-response benchmark. Its channel, angular, crossing, and analytic-continuation structure remains to be determined at the action level.

At low energy,

$$\sqrt{s} \ll E_{\rm crit} \quad \Longrightarrow \quad \mathcal{F}_L^{(4)}(s) \simeq 1. \tag{159}$$

At high energy,

$$\sqrt{s} \gg E_{\rm crit} \quad \Longrightarrow \quad \mathcal{F}_L^{(4)}(s) \simeq 16\frac{E_{\rm crit}^4}{s^2}. \tag{160}$$

The leading Higgsless longitudinal amplitude has the schematic form

$$\mathcal{M}_0(s,\theta) \sim C(s,\theta)\frac{s}{v^2}, \tag{161}$$

where $C(s,\theta)$ represents the channel and angular structure [14, 29]. The finite-formation benchmark gives

$$\mathcal{M}_{\rm HF}(s,\theta) \sim C(s,\theta)\frac{s}{v^2}\left(1 + \frac{\sqrt{s}}{2E_{\rm crit}}\right)^{-4}. \tag{162}$$

In the low-energy regime,

$$\sqrt{s} \ll E_{\rm crit} \quad \Longrightarrow \quad \mathcal{M}_{\rm HF}(s,\theta) \simeq C(s,\theta)\frac{s}{v^2}. \tag{163}$$

In the asymptotic regime,

$$\sqrt{s} \gg E_{\rm crit} \quad \Longrightarrow \quad \mathcal{M}_{\rm HF}(s,\theta) \sim 16C(s,\theta)\frac{E_{\rm crit}^4}{v^2 s}. \tag{164}$$

The four-response benchmark therefore preserves the ordinary low-energy Higgsless behavior and converts the asymptotic $s$-growth into a decreasing high-energy amplitude.

The finite-formation interpretation associates this suppression with the finite coherence length of the massive longitudinal response. As the energy increases, the causal formation scale becomes shorter than $r'_W$, and the coherent longitudinal response acquires the benchmark formation factor in Eq. (158).

### 5.1.2 Partial-Wave Consistency of the Benchmark Suppression

The $s$-wave amplitude is

$$a_0^{\rm HF}(s) = \frac{1}{32\pi}\int_{-1}^{1} d\cos\theta\, \mathcal{M}_{\rm HF}(s,\theta). \tag{165}$$

The perturbative condition is

$$\left|\mathrm{Re}\, a_0^{\rm HF}(s)\right| \le \frac{1}{2}. \tag{166}$$

[14, 29].

For the angle-independent benchmark $C = 1$,

$$a_0^{\mathrm{HF}}(s) \sim \frac{1}{16\pi}\frac{s}{v^2}\left(1+\frac{\sqrt{s}}{2E_{\mathrm{crit}}}\right)^{-4}. \tag{167}$$

Defining

$$x \equiv \frac{\sqrt{s}}{2E_{\mathrm{crit}}}, \tag{168}$$

one obtains

$$a_0^{\mathrm{HF}}(x) \sim \frac{E_{\mathrm{crit}}^2}{4\pi v^2}\frac{x^2}{(1+x)^4}. \tag{169}$$

The function

$$f(x) = \frac{x^2}{(1+x)^4} \tag{170}$$

reaches its maximum at

$$x = 1, \qquad \sqrt{s} = 2E_{\mathrm{crit}}. \tag{171}$$

Therefore,

$$a_{0,\max}^{\mathrm{HF}} \sim \frac{E_{\mathrm{crit}}^2}{64\pi v^2}. \tag{172}$$

Using

$$E_{\mathrm{crit}} \simeq 1.66\,\mathrm{TeV}, \qquad v \simeq 0.246\,\mathrm{TeV}, \tag{173}$$

gives

$$a_{0,\max}^{\mathrm{HF}} \sim \frac{(1.66)^2}{64\pi(0.246)^2} \simeq 2.26\times 10^{-1}. \tag{174}$$

This value lies below the single-channel benchmark bound $1/2$.

More generally, if the relevant channel contributes an approximately constant coefficient $C_0$, the benchmark condition becomes

$$|C_0|\frac{E_{\mathrm{crit}}^2}{64\pi v^2} \le \frac{1}{2}. \tag{175}$$

For the stated four-response benchmark, the angle-independent single-channel estimate remains below the $s$-wave perturbative bound. A complete electroweak test requires the full angular dependence, the coupled-channel partial-wave matrix, and amplitudes derived from the common non-Abelian action. The relevant channels include

$$W_L^+W_L^-, \qquad Z_LZ_L, \qquad W_L^\pm Z_L, \qquad W_L^\pm W_L^\pm, \tag{176}$$

together with the corresponding inelastic channels.

The longitudinal high-energy problem arises in interacting massive spin-one sectors because their physical longitudinal polarization vectors introduce energy-growing contributions. Massless gauge bosons contain only transverse physical polarizations, and fermions have no analogous vector-longitudinal channel [14, 15].

Table 2: Comparison of physical longitudinal polarizations and the associated massive-vector high-energy issue.

| Sector / particle | Spin | Mass | Physical longitudinal polarization? | Longitudinal-vector high-energy issue? |
|---|---|---|---|---|
| Photon $\gamma$ | 1 | massless | No | Not applicable |
| Gluon $g$ | 1 | massless | No | Not applicable |
| Weak bosons $W^{\pm}, Z^0$ | 1 | massive | Yes | Present in Higgsless interacting amplitudes unless additional cancellations or dynamics control the growth |
| Fermions $e, q, \nu$ | 1/2 | mixed | Not applicable | No vector-longitudinal channel |
| Additional massive vectors $W', Z'$ | 1 | massive | Yes | Model dependent; controlled by the gauge completion and additional unitarizing interactions or states |

### 5.2 KGC Ultraviolet Suppression and the Route Toward Perturbative Completion

The standard Klein–Gordon propagator for a relativistic scalar mode is

$$D_0(p) = \frac{i}{p^2 - m^2 + i\epsilon}. \tag{177}$$

It behaves as $p^{-2}$ at large momentum. In interacting four-dimensional field theories, this power-law behavior permits ultraviolet-divergent loop integrals for appropriate vertex structures and diagram topologies [14].

The KGC framework modifies the propagation kernel by incorporating the gravitational self-energy associated with the energy carried by a localized mode. The total-GSE finite-radius principle and the associated GSE-induced uncertainty relation provide the physical basis for this modification [30, 32].

The KGC construction first gives the magnitude-level correction

$$p_{\Lambda_m}(p) = -\beta \frac{p^3}{p_P^2} + \frac{5}{7}\beta^2 \frac{p^5}{p_P^4}, \tag{178}$$

where $p_P$ denotes the Planck momentum. This relation can be written as

$$p_{\Lambda_m}(p) = p\left[F\left(\frac{p^2}{p_P^2}\right) - 1\right], \tag{179}$$

with

$$F(x) = 1 - \beta x + \frac{5}{7}\beta^2 x^2. \tag{180}$$

The Lorentz-covariant KGC ansatz promotes this magnitude relation to the equivalent four-momentum

$$p^{\mu}_{\mathrm{eq}} = p^{\mu} F\left(\frac{p^2}{p_P^2}\right). \tag{181}$$

The promotion from the localized magnitude estimate to the covariant off-shell operator defines the constructive KGC step [30].

The corresponding scalar propagator is

$$D_{\mathrm{KGC}}(p) = \frac{i}{p^2 F^2\left(p^2/p_P^2\right) - m_{\mathrm{eq}}^2 + i\epsilon}. \tag{182}$$

For the massless sector,

$$D_{\mathrm{KGC}}^{(0)}(p) = \frac{i}{p^2 F^2\left(p^2/p_P^2\right) + i\epsilon}. \tag{183}$$

At momenta well below the Planck scale,

$$\frac{|p^2|}{p_P^2} \ll 1 \quad \Longrightarrow \quad F\left(\frac{p^2}{p_P^2}\right) \simeq 1, \tag{184}$$

and the standard Klein–Gordon propagator is recovered.

In the Euclidean large-momentum regime, the quadratic term in $F(x)$ dominates. The Euclidean propagator therefore behaves as

$$D_{\mathrm{KGC},E}(p_E) \sim \frac{1}{p_E^{10}}, \qquad p_E^2 \gg p_P^2. \tag{185}$$

The total-GSE-derived form factor increases the quadratic propagation kernel at trans-Planckian momentum and correspondingly suppresses the propagator [30].

This $p_E^{-10}$ behavior strongly improves ultraviolet power counting in scalar and compatible gauge-sector diagrams. Within a fixed local truncation of the Euclidean perturbative framework, it can render representative loop integrals ultraviolet convergent. A complete perturbative-completion claim requires the interacting vertices, gauge and ghost sectors, regularization prescription, and all relevant 1PI amplitudes to be constructed from the same action.

The real-axis pole structure follows directly from the form factor. Its discriminant is

$$\Delta_F = (-\beta)^2 - 4\left(\frac{5}{7}\beta^2\right) = -\frac{13}{7}\beta^2 < 0. \tag{186}$$

Consequently,

$$F(x) > 0 \qquad \text{for all real } x, \tag{187}$$

and the massless propagator contains no additional real-axis pole beyond $p^2 = 0$.

The additional zeros occur at

$$p_\pm^2 = \frac{7p_P^2}{10\beta}\left(1 \pm i\sqrt{\frac{13}{7}}\right), \tag{188}$$

and form a complex-conjugate pair. The KGC prescription defines the amplitudes first in the Euclidean sector and then specifies their analytic continuation. A full Lorentzian completion includes the associated contour prescription, no-pinch analysis, optical-theorem check, causality analysis, and reflection-positivity test [30, 43].

For the massless propagator, the ratio to the standard propagator is

$$G_{\mathrm{KGC}}(p^2) \equiv \frac{D_{\mathrm{KGC}}^{(0)}(p)}{D_0^{(0)}(p)} = \frac{1}{F^2\left(p^2/p_P^2\right)}, \tag{189}$$

where

$$D_0^{(0)}(p) = \frac{i}{p^2 + i\epsilon}. \tag{190}$$

For a contribution dominated by a single $s$-channel internal line with momentum $q^\mu$, one may set $q^2 = s$ as a propagator-level diagnostic:

$$G_{\mathrm{KGC}}(s) = \frac{1}{\left[1 - \beta\left(\frac{s}{p_P^2}\right) + \frac{5}{7}\beta^2\left(\frac{s}{p_P^2}\right)^2\right]^2}. \tag{191}$$

Its limiting behavior is

$$s \ll p_P^2 \quad \Longrightarrow \quad G_{\mathrm{KGC}}(s) \simeq 1, \tag{192}$$

and

$$s \gg p_P^2 \quad \Longrightarrow \quad G_{\mathrm{KGC}}(s) \sim \frac{49}{25\beta^4}\frac{p_P^8}{s^4}. \tag{193}$$

For this restricted single-line comparison,

$$\mathcal{M}_{\mathrm{line}}^{\mathrm{KGC}}(s) \sim \mathcal{M}_{\mathrm{line}}^{(0)}(s)\, G_{\mathrm{KGC}}(s). \tag{194}$$

Equation (194) acts as a propagator-level diagnostic rather than as the complete non-Abelian amplitude. The full gauge amplitude follows from the common gauge-fixed action and contains the KGC-dressed propagators, induced momentum-dependent vertices, four-point and higher-point gauge interactions, and ghost contributions.

KGC therefore provides a trans-Planckian ultraviolet-suppression principle and a candidate route toward perturbative ultraviolet completion within the specified action, contour, and gauge-completion framework. Its $p_E^{-10}$ propagator behavior governs a momentum regime far above the TeV-scale finite-formation mechanism discussed in the preceding subsection.

### 5.3 Layered High-Energy Consistency Structure

The high-energy structure assigns distinct roles to the mechanisms developed above. The physical charged-vector mass scale is assigned to electromagnetic and weak-sector self-energy [26]. The Stückelberg compensating structure provides the gauge-compatible massive-vector representation, the finite-formation principle controls the TeV-scale longitudinal response, and KGC dressing suppresses trans-Planckian propagation [28–30].

The division of physical roles is

1) charge self-energy supplies the physical mass scale of the charged weak bosons;

2) the Stückelberg compensating structure provides the gauge-compatible massive-vector representation and longitudinal coordinates;

3) the finite-formation principle converts the leading TeV-scale longitudinal growth into a bounded response that decreases asymptotically at high energy;

4) KGC dressing produces trans-Planckian ultraviolet suppression of the propagation law.

**Action-level gauge completion.** The KGC and Dirac–Choi constructions provide Abelian action-level prototypes for gauge-covariant operator dressing and Ward–Takahashi control [30, 41].

The finite-formation factor acts on complete physical longitudinal amplitudes or gauge-invariant coupled-channel eigenamplitudes as described in Subsection 5.1, while KGC controls the trans-Planckian propagation law described in Subsection 5.2.

The layered structure therefore connects four distinct physical functions: mass origin, massive-vector gauge representation, TeV-scale longitudinal control, and trans-Planckian ultraviolet suppression. Their common non-Abelian embedding follows the gauge-completion conditions summarized in Subsection 4.3, while the finite-formation and KGC mechanisms retain the distinct momentum-space roles described above.

# 6 Minimal Effective Self-Energy Framework

## 6.1 Schematic Effective Lagrangian Architecture

The preceding sections assign the charged weak-boson mass scale to electromagnetic and weak-sector self-energy, organize the massive-vector representation through Stückelberg compensating fields, describe the neutral massive states as $W^+W^-$ composite resonances, and separate the TeV-scale finite-formation response from trans-Planckian KGC dressing [26–28, 30, 41].

The present effective construction is written in the physical mass-eigenstate basis. A schematic organization is

$$\mathcal{L}_{\rm SE}^{\rm BP} = \mathcal{L}_{\gamma W}^{\rm KGC} + \mathcal{L}_{\rm fermion}^{\rm DC} + \mathcal{L}_{\rm St,lin}^{W} + \mathcal{L}_{Z,X}^{\rm comp} + \mathcal{L}_{\rm int}^{\rm BP} + \Delta\mathcal{L}_{\rm form}^{\rm eff}. \tag{195}$$

The superscript BP denotes the broken-phase effective representation, while SE denotes the self-energy framework.

The KGC form factor and quadratic dressing kernel are

$$F(x) = 1 - \beta x + \frac{5}{7}\beta^2 x^2, \qquad \mathcal{K}_{\rm KGC}(x) \equiv F^2(x), \qquad x = -\frac{\Box}{p_P^2}. \tag{196}$$

The infrared limit recovers the ordinary quadratic kernel, while the $R = 2$ form produces the trans-Planckian suppression described in Section 5.2 [30].

The photon and charged-vector kinetic sector is written schematically as

$$\mathcal{L}_{\gamma W}^{\rm KGC} = -\frac{1}{4}F_{\mu\nu}\mathcal{K}_{\rm KGC}\left(-\frac{\Box}{p_P^2}\right)F^{\mu\nu} - \frac{1}{2}W_{\mu\nu}^{+}\mathcal{K}_{\rm KGC}\left(-\frac{\mathcal{D}^2}{p_P^2}\right)W^{-\mu\nu}, \tag{197}$$

with the standard $U(1)_{\rm em}$-covariant charged-vector field strength. This expression displays the KGC-dressed quadratic propagation in the broken-phase representation.

The fermion sector adopts the gauge-covariant Dirac–Choi structure,

$$\mathcal{L}_{\rm fermion}^{\rm DC} = \sum_f \left\{ \frac{i}{2}\bar{f}\gamma^\mu \left[ \mathcal{D}_\mu^{(f)} F\left(-\frac{(\mathcal{D}^{(f)})^2}{p_P^2}\right) - F\left(-\frac{(\overleftarrow{\mathcal{D}}^{(f)})^2}{p_P^2}\right)\overleftarrow{\mathcal{D}}_\mu^{(f)} \right] f - m_f^{\rm SE}\bar{f}f \right\}, \tag{198}$$

where

$$\mathcal{D}_\mu^{(f)} = \partial_\mu + ieQ_f A_\mu. \tag{199}$$

The symmetric operator placement gives a real action and generates the correlated momentum-dependent vertices and induced multi-photon vertices of the Abelian Dirac–Choi construction [41]. The parameters $m_f^{\rm SE}$ represent broken-phase physical mass parameters associated with fermion self-energy and internal dynamics.

The charged weak-vector mass sector uses the linearized Stückelberg representation

$$\mathcal{L}^{W}_{\mathrm{St,lin}} = \left(M_W^{\mathrm{SE}} W^{+}_{\mu} - \mathcal{D}_{\mu}\pi^{+}\right)\left(M_W^{\mathrm{SE}} W^{-\mu} - \mathcal{D}^{\mu}\pi^{-}\right), \tag{200}$$

with

$$\mathcal{D}_{\mu}\pi^{\pm} = \left(\partial_{\mu} \pm ieA_{\mu}\right)\pi^{\pm}. \tag{201}$$

The fields $\pi^{\pm}$ provide compensating longitudinal coordinates [27, 28], while $M_W^{\mathrm{SE}}$ carries the charged weak-boson rest-energy scale obtained from electromagnetic and weak-sector self-energy [26].

The neutral massive sector is represented by effective composite fields,

$$\begin{aligned}\mathcal{L}^{\mathrm{comp}}_{Z,X} = &-\frac{1}{4}Z_{\mu\nu}\mathcal{K}_{\mathrm{KGC}}\left(-\frac{\Box}{p_P^2}\right)Z^{\mu\nu} + \frac{1}{2}M_Z^2 Z_{\mu}Z^{\mu} \\ &-\frac{1}{2}X_1^0\left[\Box\mathcal{K}_{\mathrm{KGC}}\left(-\frac{\Box}{p_P^2}\right) + M_{X_1}^2\right]X_1^0.\end{aligned} \tag{202}$$

Here $Z_{\mu}$ represents the lowest $W^{+}W^{-}$ composite vector pole, while $X_1^0$ represents the first radially excited scalar channel, identified with $X_1^0(125)$ [26]. The Proca-type $Z_{\mu}$ term is used as the low-energy pole representation of the composite vector resonance.

The remaining interaction term,

$$\mathcal{L}^{\mathrm{BP}}_{\mathrm{int}} = \mathcal{L}^{\mathrm{eff}}_{Z} + \mathcal{L}^{\mathrm{eff}}_{X} + \cdots, \tag{203}$$

contains the broken-phase couplings of the composite neutral states and is specified in Subsection 6.2.

The term

$$\Delta\mathcal{L}^{\mathrm{eff}}_{\mathrm{form}} \tag{204}$$

denotes the gauge-correlated operator sector whose physical $2 \to 2$ reduction produces the finite-formation factor introduced in Subsection 5.1.

## 6.2 Effective Couplings of the Composite Neutral Sector

The physical neutral massive sector is represented by composite fields associated with the $W^{+}W^{-}$ system. The observed $Z^0$ is assigned to the lowest vector channel and $X_1^0(125)$ to the first radially excited scalar channel [26]. Their masses and spectroscopic assignments were specified in Section 2.3.

The effective interaction of the composite neutral vector is

$$\mathcal{L}^{\mathrm{eff}}_{Z} = \mathcal{L}^{\mathrm{eff}}_{ZWW} + g_Z^{\mathrm{ref}} Z_{\mu}\sum_{f}\bar{f}\gamma^{\mu}\left(g_V^f - g_A^f\gamma^5\right)f, \tag{205}$$

where

$$\begin{aligned}\mathcal{L}^{\mathrm{eff}}_{ZWW} = -ig^{\mathrm{eff}}_{ZWW}\Big[&\left(W^{+}_{\mu\nu}W^{-\mu} - W^{-}_{\mu\nu}W^{+\mu}\right)Z^{\nu} \\ &+ W^{+}_{\mu}W^{-}_{\nu}Z^{\mu\nu}\Big] + \cdots.\end{aligned} \tag{206}$$

Here $g_Z^{\mathrm{ref}}$ denotes the conventional neutral-current normalization defined explicitly in Subsection 7.1.

The vector and axial couplings are parameterized by

$$g_V^f = \left(g_V^f\right)_{\rm ref} + \delta g_V^f, \qquad g_A^f = \left(g_A^f\right)_{\rm ref} + \delta g_A^f, \tag{207}$$

where the deviations are constrained by pole asymmetries, partial widths, and low-energy neutral-current observables [15].

The leading CP-even interactions of the scalar composite channel are

$$\begin{aligned}\mathcal{L}_X^{\rm eff} = {} & g_{XWW}^{\rm eff} X_1^0 W_\mu^+ W^{-\mu} + \frac{1}{2} g_{XZZ}^{\rm eff} X_1^0 Z_\mu Z^\mu - \sum_f y_{Xf}^{\rm eff} X_1^0 \bar{f} f \\ & + \frac{1}{2} c_{WW}^{\rm eff} X_1^0 W_{\mu\nu}^+ W^{-\mu\nu} + \frac{1}{4} c_{ZZ}^{\rm eff} X_1^0 Z_{\mu\nu} Z^{\mu\nu} \\ & + \frac{1}{2} c_{Z\gamma}^{\rm eff} X_1^0 Z_{\mu\nu} F^{\mu\nu} + \frac{1}{4} c_{\gamma\gamma}^{\rm eff} X_1^0 F_{\mu\nu} F^{\mu\nu} \\ & + \frac{1}{4} c_{gg}^{\rm eff} X_1^0 G_{\mu\nu}^A G^{A\mu\nu} + \cdots . \end{aligned} \tag{208}$$

Here $y_{Xf}^{\rm eff}$ is a composite-resonance coupling and is independent of the self-energy mechanism used to parameterize the fermion rest-energy scale.

Dimensionless coupling modifiers are defined by

$$\kappa_W^X = \frac{g_{XWW}^{\rm eff}}{2m_W^2/v_F}, \qquad \kappa_Z^X = \frac{g_{XZZ}^{\rm eff}}{2M_Z^2/v_F}, \qquad \kappa_f^X = \frac{y_{Xf}^{\rm eff}}{m_f/v_F}, \tag{209}$$

where

$$v_F = \left(\sqrt{2} G_F\right)^{-1/2} \tag{210}$$

is the conventional electroweak normalization scale [15, 38].

The observable signal strength for production channel $P$ and decay channel $D$ is

$$\mu_{P,D} = \frac{\sigma_P(pp \to X_1^0)\,{\rm BR}(X_1^0 \to D)}{[\sigma_P(pp \to h)\,{\rm BR}(h \to D)]_{\rm SM}}. \tag{211}$$

Finite composite structure may be represented by vertex form factors,

$$g_{XAB}^{\rm eff} \quad \longrightarrow \quad g_{XAB}^{\rm eff} \mathcal{F}_{XAB}\left(q^2, p_A^2, p_B^2\right). \tag{212}$$

The local effective coupling is defined at a channel-dependent reference point,

$$\mathcal{F}_{XAB}\left(M_{X_1}^2, \bar{p}_A^2, \bar{p}_B^2\right) = 1. \tag{213}$$

Here $\bar{p}_A^2$ and $\bar{p}_B^2$ denote the reference virtualities used for the channel. At momentum transfers comparable to the inverse composite-size scale, $\mathcal{F}_{XAB}$ parameterizes finite-size and off-shell effects.

The width hierarchy may likewise be parameterized through constituent overlap and channel-dependent decay matrix elements, while a microscopic $W^+W^-$ calculation must determine the corresponding wave functions, matrix elements, and widths [15, 38, 44].

An illustrative wave-packet overlap benchmark for this width hierarchy is given in Appendix B.

Precision neutral-current observables constrain the $Z^0$ channel, while production rates, branching ratios, angular distributions, and off-shell form factors test the $X_1^0(125)$ channel [15, 38]. These tests are developed in Section 7.

### 6.3 Scope of the Effective Construction

The present construction is a broken-phase mass-eigenstate effective architecture rather than the final $SU(2)_L \times U(1)_Y$ action. It combines KGC-dressed gauge propagation, Dirac–Choi fermion propagation, the charged-sector Stückelberg representation, composite neutral poles, and the finite-formation principle in the form summarized by Eq. (195).

A complete electroweak realization must embed the fermions in their chiral multiplets, produce the massless photon and observed neutral currents, and generate the composite $Z^0$ pole without an additional elementary neutral massive pole.

The role of the present effective construction is therefore to provide the field-theoretic language for phenomenological tests of the proposed self-energy mass origin and composite neutral spectrum. Its complete chiral and non-Abelian realization constitutes the subsequent action-level stage.

## 7 Phenomenological Tests and Falsifiability

The present framework is tested through four complementary experimental directions: precision neutral-current observables, the production and decay properties of $X_1^0(125)$, searches for the additional neutral candidate $X_2^0$, and polarization-sensitive vector-boson scattering.

### 7.1 Precision Neutral-Current Constraints

The neutral-current sector provides a stringent precision test of the composite $Z^0$ interpretation. The observed $Z^0$ resonance is assigned to the lowest neutral vector channel of the underlying $W^+W^-$ system [26].

The effective fermionic interaction is written as

$$\mathcal{L}^{\text{eff}}_{Zff} = g_Z^{\text{ref}} Z_\mu \sum_f \bar{f}\gamma^\mu \left[ g_V^f(q^2) - g_A^f(q^2)\gamma^5 \right] f, \tag{214}$$

where

$$g_Z^{\text{ref}} \equiv M_Z \left(\sqrt{2} G_F\right)^{1/2}. \tag{215}$$

In the conventional tree-level electroweak parameterization this normalization equals $g/(2c_W)$.

The pole couplings are parameterized as

$$g_{V,A}^f(M_Z^2) = \left(g_{V,A}^f\right)_{\text{ref}} + \delta g_{V,A}^f, \tag{216}$$

where the reference values denote the conventional radiatively corrected electroweak couplings.

For $M_Z \gg m_f$, the leading partial width is

$$\Gamma_f \simeq N_c^f \frac{G_F M_Z^3}{6\sqrt{2}\pi} \Big[ |g_V^f(M_Z^2)|^2 (1 + \Delta_V^f) + |g_A^f(M_Z^2)|^2 (1 + \Delta_A^f) \Big], \tag{217}$$

where the $\Delta_{V,A}^f$ terms collect the relevant radiative and fermion-mass corrections [14, 15].

Additional decay channels are separated from shifts of the known fermionic vertices through

$$\Gamma_Z = \sum_{f \in \text{known}} \Gamma_f + \Gamma_Z^{\text{new}}, \qquad \Gamma_{\text{inv}} = \sum_{i=1}^{3} \Gamma_{\nu_i} + \Gamma_{\text{inv}}^{\text{new}}. \tag{218}$$

The pole asymmetry parameter is

$$\mathcal{A}_f = \frac{2\,\mathrm{Re}\left[g_V^f(M_Z^2)g_A^{f*}(M_Z^2)\right]}{|g_V^f(M_Z^2)|^2 + |g_A^f(M_Z^2)|^2}, \tag{219}$$

and for charged leptons

$$\mathrm{Re}\left[\frac{g_V^\ell(M_Z^2)}{g_A^\ell(M_Z^2)}\right] = 1 - 4\sin^2\theta_{\mathrm{eff}}^\ell. \tag{220}$$

Widths and asymmetries therefore constrain complementary combinations of the vector and axial couplings [15].

Finite composite structure may also generate off-pole momentum dependence, which is parameterized near the $Z$ pole as

$$g_{V,A}^f(q^2) = g_{V,A}^f(M_Z^2) + \eta_{V,A}^f \frac{(q^2 - M_Z^2)R_Z^2}{(\hbar c)^2} + \cdots. \tag{221}$$

The PDG 2024 Breit–Wigner mass and width benchmarks include

$$M_Z^{\mathrm{BW}} = 91.1880 \pm 0.0020\,\mathrm{GeV}, \tag{222}$$
$$\Gamma_Z = 2.4955 \pm 0.0023\,\mathrm{GeV}, \tag{223}$$
$$\Gamma_{\ell\ell} = 83.984 \pm 0.086\,\mathrm{MeV}, \tag{224}$$
$$\Gamma_{\mathrm{inv}} = 499.3 \pm 1.5\,\mathrm{MeV} \tag{225}$$

[15]. A microscopic calculation formulated in terms of a complex pole must be converted to the same resonance convention before comparison.

The width measurements reach observable-level precisions of order $10^{-3}$, but bounds on individual $\delta g_V^f$, $\delta g_A^f$, and off-pole slope parameters require a correlated fit to widths, asymmetries, flavor ratios, and off-pole data. Predictions outside the experimentally allowed global region exclude the corresponding composite $Z^0$ realization.

## 7.2 Signal Strengths of the $X_1^0(125)$ Scalar Resonance

The 125 GeV scalar resonance provides a central test of the composite interpretation. The present spectrum assigns it to the $n_r = 1$, $J^P = 0^+$ channel of the $W^+W^-$ system and denotes it by $X_1^0(125)$ [26].

For production category $P$ and decay channel $D$, the signal strength is

$$\mu_{P,D}^X = \frac{\sigma_P(pp \to X_1^0)\,\mathrm{BR}(X_1^0 \to D)}{[\sigma_P(pp \to h_{\mathrm{ref}})\,\mathrm{BR}(h_{\mathrm{ref}} \to D)]_{m_{h_{\mathrm{ref}}} = M_{X_1}}}. \tag{226}$$

The denominator is the Standard Model reference rate evaluated at the same resonance mass [38, 45].

The effective couplings and form factors entering the production and decay amplitudes are defined in Subsection 6.2. In the narrow-width approximation, the signal strength takes the factorized form

$$\mu_{P,D}^X = \frac{\sigma_P^X}{\sigma_P^{\mathrm{ref}}} \frac{\Gamma_D^X}{\Gamma_D^{\mathrm{ref}}} \frac{\Gamma_{\mathrm{tot}}^{\mathrm{ref}}}{\Gamma_{\mathrm{tot}}^X}, \tag{227}$$

with

$$\Gamma_{\mathrm{tot}}^X = \sum_{D \in \mathrm{SM}} \Gamma_D^X + \Gamma_{\mathrm{inv}}^X + \Gamma_{\mathrm{exotic}}^X. \tag{228}$$

Derivative interactions and composite form factors can modify differential kinematics and experimental acceptance, so the full test uses correlated production and decay information rather than independent comparisons of individual couplings [38, 45].

As a representative inclusive benchmark, the ATLAS full Run 2 combination under a common-signal-strength assumption gives [45]

$$\mu_{\text{global}} = 1.05 \pm 0.06. \tag{229}$$

The microscopic $W^+W^-$ calculation must ultimately predict the correlated production rates, partial widths, form factors, and total width. A prediction outside the experimentally allowed combined likelihood excludes the corresponding $X_1^0(125)$ composite realization.

### 7.3 Search Window for an Additional Neutral Resonance Near 135.4 GeV

The radial-excitation analysis selects an additional neutral candidate $X_2^0$. Its radial assignment and search interval are

$$n_r = 2, \tag{230}$$

$$133.7\,\text{GeV} \lesssim M_{X_2}c^2 \lesssim 138.2\,\text{GeV}, \tag{231}$$

$$M_{X_2}^{\text{bench}}c^2 \simeq 135.4\,\text{GeV}. \tag{232}$$

The interval follows from the geometric radial extrapolation rather than from a uniquely calculated eigenvalue [26].

The total spin remains open. For low orbital angular momentum, scalar, vector, and tensor assignments are possible. An on-shell spin-one state cannot decay into two real photons, so a vector hypothesis must be tested through other channels [46, 47].

For each production and decay hypothesis, the direct experimental observable is

$$\mathcal{R}_{P,D}^{X_2^0} \equiv \sigma_P(pp \to X_2^0)\,\text{BR}(X_2^0 \to D). \tag{233}$$

Relevant final states include $\gamma\gamma$, $ZZ^*$, $WW^*$, $Z\gamma$, $b\bar{b}$, and $\tau^+\tau^-$, subject to the corresponding spin–parity selection rules.

For a common final state $D$, the resonance search must allow for interference,

$$\frac{d\sigma_D}{dm} \propto \left|\mathcal{A}_{\text{cont}}^D + \mathcal{A}_{X_1^0}^D + \mathcal{A}_{X_2^0}^D\right|^2. \tag{234}$$

The cited ATLAS and CMS low-mass diphoton searches extend only to 110 GeV, while the cited heavy-diphoton search begins at 150 GeV. They therefore do not directly cover the proposed 133.7–138.2 GeV interval [48–50].

Null searches constrain $\sigma_P\text{BR}_D$ for specified production, decay, width, and spin hypotheses. Conversely, a resonance in the predicted mass interval supports the proposed composite sequence only if its width, production pattern, branching fractions, and angular properties are jointly compatible with one $W^+W^-$ assignment.

### 7.4 Vector-Boson Scattering

Vector-boson scattering provides the direct TeV-scale test of the finite-formation principle. In a Higgsless electroweak effective theory, longitudinal weak-boson amplitudes exhibit energy growth in the TeV regime [14, 29]. The present benchmark modifies this behavior through the formation factor derived in Subsection 5.1.

Collider predictions must be embedded in the full electroweak process $pp \to jj\,4f$, with a specified polarization definition and interference treatment [51, 52].

For the four-longitudinal-response benchmark,

$$E_{\rm crit} = \frac{\hbar c}{2r'_W} \simeq 1.66\,\text{TeV}, \qquad r'_W \simeq 5.93 \times 10^{-20}\,\text{m}, \tag{235}$$

$$\mathcal{F}^{(4)}_{LLLL}(\hat{s}_{VV}) = \left(1 + \frac{\sqrt{\hat{s}_{VV}}}{2E_{\rm crit}}\right)^{-4}. \tag{236}$$

The corresponding projected helicity amplitude is

$$\mathcal{M}_{\text{SE},LLLL} = \mathcal{M}_{0,LLLL}\,\mathcal{F}^{(4)}_{LLLL}. \tag{237}$$

The suppression relative to the unsuppressed Higgsless $LLLL$ benchmark is

$$r^{\rm form}_{LLLL}(\hat{s}_{VV}) = \left|\mathcal{F}^{(4)}_{LLLL}(\hat{s}_{VV})\right|^2 = \left(1 + \frac{\sqrt{\hat{s}_{VV}}}{2E_{\rm crit}}\right)^{-8}. \tag{238}$$

For $E_{\rm crit} = 1.66\,\text{TeV}$,

$$r^{\rm form}_{LLLL} \simeq 1.22 \times 10^{-1}, \qquad \sqrt{\hat{s}_{VV}} = 1\,\text{TeV}, \tag{239}$$

$$r^{\rm form}_{LLLL} \simeq 2.30 \times 10^{-2}, \qquad \sqrt{\hat{s}_{VV}} = 2\,\text{TeV}, \tag{240}$$

$$r^{\rm form}_{LLLL} \simeq 5.80 \times 10^{-3}, \qquad \sqrt{\hat{s}_{VV}} = 3\,\text{TeV}. \tag{241}$$

These factors describe suppression relative to the unsuppressed Higgsless longitudinal benchmark, not directly relative to the Standard Model. The observable prediction must be obtained from the complete electroweak amplitude including transverse and mixed polarizations, decays, nonresonant contributions, and interference.

The experimentally relevant channels include same-sign $WWjj$, opposite-sign $WWjj$, $WZjj$, and $ZZjj$ [53, 54]. ATLAS reports an observed 95% confidence-level upper limit of 0.45 fb for the doubly longitudinal same-sign $WWjj$ fiducial component, while the earlier CMS analysis reported 1.17 fb [55, 56].

The finite-formation construction becomes quantitatively falsifiable when the common non-Abelian action fixes the absolute polarization-resolved distributions. A correlated comparison across the $WW$, $WZ$, and $ZZ$ channels then tests the predicted high-energy deformation.

### 7.5 Scope of the First-Stage Construction

The present paper establishes the first stage of a Higgs-free electroweak replacement program. It formulates the self-energy origin of the charged weak-boson mass scale, the $W^+W^-$ composite interpretation of the neutral massive sector, the Stückelberg-compatible massive-vector representation, the finite-formation principle, and the resulting phenomenological tests. A complete chiral, flavor, and non-Abelian realization belongs to a subsequent stage of the program.

Table 3 summarizes the principal developments beyond the present construction.

The present construction therefore defines a testable first-stage architecture whose microscopic binding and complete non-Abelian realization constitute the principal next theoretical steps.

## 8 Conclusion

The Standard Model Higgs sector provides an internally consistent and empirically successful description of electroweak symmetry breaking and the observed 125 GeV scalar resonance. Its

Table 3: Principal next-stage developments beyond the present first-stage Higgs-free electroweak construction.

| **Next stage** | **Main task** |
|---|---|
| Microscopic mass dynamics | Derive the $W^{\pm}$ and fermion rest-energy scales from normalized source distributions, self-energy integrals, internal dynamics, and binding contributions. |
| Composite spectroscopy | Derive the $W^+W^-$ binding equation, normalized wave functions, radial structure, pole properties, widths, and branching fractions, and determine the detailed properties of the additional $X_2^0$ candidate. |
| Gauge completion | Construct the chiral non-Abelian electroweak action with correlated propagators, three-point, four-point, and higher-point vertices, gauge-fixing and ghost sectors, BRST transformations, and Slavnov–Taylor consistency. |
| Phenomenology | Perform correlated tests using precision neutral-current observables, the production and decay properties of $X_1^0(125)$, dedicated searches for $X_2^0$, and vector-boson-scattering observables. |

parameters nevertheless leave open the deeper microscopic origin of the electroweak scale, the scalar mass, and the fermion Yukawa hierarchy [14, 15]. These questions motivate the investigation of testable alternatives to a fundamental Higgs condensate.

The present work establishes the first stage of a Higgs-free electroweak replacement program based on self-energy and composite dynamics. The charged weak-boson rest-energy scale is assigned primarily to electromagnetic and weak-sector self-energy,

$$M_W^{\mathrm{SE}}c^2 \simeq U_{\mathrm{em}}^{(W)} + U_{\mathrm{weak}}^{(W)} + \cdots . \tag{242}$$

Stückelberg compensating fields then organize the resulting massive weak-vector sector in a gauge-compatible representation and parameterize its longitudinal degrees of freedom [27, 28]. In this construction, the physical origin of the mass scale and its gauge representation are treated as distinct structural elements.

The neutral massive sector is organized as a $W^+W^-$ composite spectrum. The observed $Z^0$ resonance is assigned to

$$(n_r, S, L, J) = (0, 1, 0, 1), \tag{243}$$

while the observed scalar resonance $X_1^0(125)$ is assigned to

$$(n_r, S, L, J) = (1, 0, 0, 0). \tag{244}$$

Their effective mass relations are

$$M_Z c^2 = 2M_W^{\mathrm{SE}}c^2 + U_{\mathrm{binding}}^{(Z)}, \qquad M_{X_1}c^2 = 2M_W^{\mathrm{SE}}c^2 + U_{\mathrm{binding}}^{(X_1)}. \tag{245}$$

The geometrically inferred radial ordering further selects an additional neutral candidate $X_2^0$ with

$$n_r = 2, \qquad 133.7\,\mathrm{GeV} \lesssim M_{X_2}c^2 \lesssim 138.2\,\mathrm{GeV}, \tag{246}$$

with 135.4 GeV serving as a representative benchmark rather than a uniquely calculated eigenvalue [26].

The framework separates its high-energy behavior into two physically distinct regimes. At the TeV scale, the finite-formation principle introduces the characteristic scale

$$E_{\mathrm{crit}} = \frac{\hbar c}{2r'_W} \simeq 1.66\,\mathrm{TeV}, \qquad r'_W \simeq 5.93 \times 10^{-20}\,\mathrm{m}, \tag{247}$$

and the four-response benchmark

$$\mathcal{F}^{(4)}_{LLLL}(\hat{s}_{VV}) = \left(1 + \frac{\sqrt{\hat{s}_{VV}}}{2E_{\mathrm{crit}}}\right)^{-4}. \tag{248}$$

This benchmark converts the leading Higgsless $\hat{s}_{VV}$-growth into a bounded longitudinal response that decreases asymptotically with the vector-boson subprocess energy [26, 29]. Its complete channel, polarization, crossing, and off-shell structure remains to be derived from the common non-Abelian action.

At trans-Planckian momentum, KGC and Dirac–Choi dressing provide the separate ultraviolet layer. For the $R = 2$ realization, the Euclidean large-momentum propagators behave as

$$D_{\mathrm{scalar/gauge},E}(p_E) \sim p_E^{-10}, \qquad S_{\mathrm{spinor},E}(p_E) \sim p_E^{-5}, \qquad p_E^2 \gg p_P^2. \tag{249}$$

These behaviors provide strong trans-Planckian propagation suppression within the specified fixed-truncation framework [30, 41]. The TeV-scale finite-formation principle and the trans-Planckian KGC mechanism therefore address distinct high-energy problems.

The resulting model is directly testable. Precision neutral-current observables constrain the composite $Z^0$ channel, while the measured production and decay properties of $X_1^0(125)$ constrain the composite scalar interpretation [15, 38, 45]. Vector-boson scattering tests the finite-formation principle [55,56], while dedicated resonance searches in the 133.7–138.2 GeV interval provide a direct test of the predicted $X_2^0$ candidate [26].

The present work therefore provides a concrete first-stage alternative to the fundamental-Higgs organization of electroweak mass and neutral spectroscopy. Its central result is the combined structure of self-energy mass generation, $W^+W^-$ composite neutral states, Stückelberg-compatible massive-vector representation, finite-formation longitudinal control, and KGC ultraviolet suppression. A microscopic $W^+W^-$ composite calculation and a BRST-controlled non-Abelian electroweak realization constitute the next theoretical stage. The precision neutral-current observables, $X_1^0(125)$ properties, vector-boson scattering, and the $X_2^0$ search interval provide direct experimental routes for discriminating this framework from the conventional fundamental-Higgs interpretation.

**Acknowledgements.** The specific self-energy electroweak construction developed in this paper, the $W^+W^-$ composite interpretation of the $Z^0$ and $X_1^0(125)$ states, the proposed $X_2^0$ ($133.7\,\mathrm{GeV} \lesssim M_{X_2}c^2 \lesssim 138.2\,\mathrm{GeV}$) search interval, the finite-formation principle, and their integration with the KGC framework are original contributions of the author. Parts of the exposition and LaTeX drafting were assisted by a generative AI language model. The author reviewed the equations, derivations, and physical claims and assumes full responsibility for the final manuscript.

## A Illustrative Quark-Scale Mapping of the Self-Energy Ansatz

Quarks carry both electric charge and color charge. The quark sector therefore provides an illustrative numerical application of the self-energy ansatz. We first retain only the electro-

static contribution and then introduce an effective strong-sector term motivated by the radial structure of the Cornell potential.

The representative quark-mass parameters used below are renormalized quantities whose values depend on the mass scheme and scale. The calculated lengths consequently inherit the conventions of the numerical inputs [14, 15, 26].

### A.1 Electrostatic Effective Length Scales

The first approximation retains only the electrostatic contribution,

$$m_q c^2 \approx U_{\rm es}. \tag{250}$$

For a uniformly charged sphere with $Q_e = q_q e$,

$$U_{\rm es} = \beta_{\rm em} \frac{\alpha_{\rm em} \hbar c \, q_q^2}{R_{\rm es}}, \qquad \beta_{\rm em} = \frac{3}{5}, \tag{251}$$

and therefore

$$R_{\rm es} = \frac{3}{5} \frac{\alpha_{\rm em} \hbar c \, q_q^2}{m_q c^2}. \tag{252}$$

The electric-charge factors are

$$q_u = q_c = q_t = \frac{2}{3}, \qquad q_d = q_s = q_b = -\frac{1}{3}. \tag{253}$$

Using

$$\alpha_{\rm em} \hbar c \simeq 1.439964 \, \text{MeV fm}, \tag{254}$$

together with the representative mass inputs adopted in the preceding analysis, Eq. (252) gives the effective electrostatic length scales listed in Table 4 [15, 26].

Table 4: Effective electrostatic length scales obtained from Eq. (252). The mass values are representative renormalized quark-mass inputs.

| Quark | Representative mass input (MeV/$c^2$) | $R_{\rm es}$ (m) |
|---|---|---|
| Up | $\approx 2.2$ | $\approx 1.7 \times 10^{-16}$ |
| Down | $\approx 4.7$ | $\approx 2.0 \times 10^{-17}$ |
| Strange | $\approx 95$ | $\approx 1.0 \times 10^{-18}$ |
| Charm | $\approx 1{,}270$ | $\approx 3.0 \times 10^{-19}$ |
| Bottom | $\approx 4{,}180$ | $\approx 2.3 \times 10^{-20}$ |
| Top | $\approx 173{,}000$ | $\approx 2.2 \times 10^{-21}$ |

Equation (252) maps the observed quark-mass hierarchy into an inverse hierarchy of effective electrostatic scales. Within each electric-charge family, $R_{\rm es} \propto m_q^{-1}$, while the factor $q_q^2$ distinguishes the up-type and down-type sectors. These quantities are the characteristic length parameters of the electrostatic self-energy ansatz rather than independently measured hard quark radii.

### A.2 An Extended Phenomenological Ansatz with a Strong-Sector Term

The standard Cornell potential for a heavy color-singlet $q\bar{q}$ system is

$$V_{\rm Cornell}(r) = -\frac{\kappa}{r} + \sigma r \qquad (\hbar = c = 1), \tag{255}$$

combining a short-distance Coulomb-like term with a linear confining term [35, 36].

The present one-body self-energy model adopts the same inverse-radius and linear radial structures and assigns them the effective form

$$U_{\rm ss}^{\rm eff}(R) = +\frac{A}{R} - \sigma_{\rm fm} R. \tag{256}$$

In the present phenomenological ansatz, the positive inverse-radius term is assigned to an effective short-distance color self-energy contribution, while the negative linear term parameterizes an effective strong-interaction binding contribution [26].

Adding the electrostatic term gives

$$m_q c^2 \approx \beta_{\rm em} \frac{\alpha_{\rm em} \hbar c\, q_q^2}{R} + \frac{A}{R} - \sigma_{\rm fm} R, \qquad \beta_{\rm em} = \frac{3}{5}. \tag{257}$$

For the numerical benchmark, we use

$$A = 98.65\,\text{MeV fm}, \qquad \sigma = 0.18\,\text{GeV}^2, \qquad \sigma_{\rm fm} \equiv \frac{\sigma}{\hbar c} \simeq 0.912\,\text{GeV/fm}, \tag{258}$$

following the parameter choice adopted in the preceding analysis [26].

Multiplying Eq. (257) by $R$ gives

$$\sigma_{\rm fm} R^2 + (m_q c^2) R - \left(\beta_{\rm em} \alpha_{\rm em} \hbar c\, q_q^2 + A\right) = 0. \tag{259}$$

The positive solution is

$$R_q = \frac{-m_q c^2 + \sqrt{(m_q c^2)^2 + 4\sigma_{\rm fm}\left(\beta_{\rm em} \alpha_{\rm em} \hbar c\, q_q^2 + A\right)}}{2\sigma_{\rm fm}}. \tag{260}$$

The resulting effective scales are listed in Table 5.

Table 5: Effective quark length scales obtained from the electrostatic and strong-sector ansatz in Eq. (257).

| Quark | Representative mass input (MeV/$c^2$) | $R_q$ (fm) |
|---|---|---|
| Up | $\approx 2.2$ | $\approx 0.328$ |
| Down | $\approx 4.7$ | $\approx 0.326$ |
| Strange | $\approx 95$ | $\approx 0.281$ |
| Charm | $\approx 1{,}270$ | $\approx 0.0740$ |
| Bottom | $\approx 4{,}180$ | $\approx 0.0235$ |
| Top | $\approx 173{,}000$ | $\approx 5.72 \times 10^{-4}$ |

Equation (260) yields one positive effective scale for each mass input. All of the extracted scales are smaller than the characteristic nucleon size, $R_N \sim 0.8\,\text{fm}$, placing them in the sub-nucleonic regime. Within the present phenomenological ansatz, this hierarchy is consistent with interpreting $R_q$ as a compact dressed-source scale rather than as a nucleon-sized structure [15, 57]. In the light-quark sector, the common strong-sector coefficients dominate the solution and bring the up- and down-quark scales close together despite their different electric charges. In the heavy-mass limit,

$$R_q \simeq \frac{\beta_{\rm em} \alpha_{\rm em} \hbar c\, q_q^2 + A}{m_q c^2}, \tag{261}$$

so the effective scale decreases approximately inversely with the input mass.

The two calculations establish a direct mapping between the quark-mass parameters and the characteristic length scales of the self-energy ansatz. A microscopic completion requires the effective strong contribution $U_{\rm ss}^{\rm eff}(R)$ to be derived from a gauge-invariant QCD description of the dressed quark state.

## B Wave-Packet Overlap Benchmark for the Neutral-State Width Hierarchy

The measured $Z^0$ width and the conventional narrow-width reference for the 125 GeV scalar define a useful phenomenological hierarchy [15]:

$$\Gamma_Z = 2.4955 \pm 0.0023\,\text{GeV}, \qquad \Gamma_X^{\text{ref}} \simeq 4.1\,\text{MeV}. \tag{262}$$

The scalar value is used here as a phenomenological target rather than as a model-independent direct measurement of the composite-state width. Indirect experimental extractions are compatible with a few-MeV scale but depend on assumptions relating on-shell and off-shell effective couplings [15].

The corresponding width ratio is

$$\frac{\Gamma_X^{\text{ref}}}{\Gamma_Z} \simeq 1.64 \times 10^{-3} \simeq \frac{1}{609}. \tag{263}$$

Since an approximately exponential decay law gives $\tau \simeq \hbar/\Gamma$, the corresponding reference lifetime ratio is $\tau_X^{\text{ref}}/\tau_Z \simeq 609$.

In the present composite interpretation, a possible spatial contribution to this hierarchy arises from the different internal configurations of the first two neutral $W^+W^-$ levels. The $Z^0$ is assigned to a compact vector configuration and $X_1^0(125)$ to a more extended scalar configuration [26]. Using the refined characteristic distances,

$$d_Z \simeq 1.89 r'_W, \qquad d_X \simeq 3.57 r'_W, \tag{264}$$

where $d_Z$ and $d_X$ denote constituent-center separations.

For a transition kernel localized over a distance shorter than the constituent wave-packet scale, define the normalized density overlap

$$\widehat{\mathcal{O}}(d) \equiv \frac{\displaystyle\int d^3x\, \rho_{W^+}(\mathbf{x})\rho_{W^-}(\mathbf{x};d)}{\displaystyle\int d^3x\, \rho_W^2(\mathbf{x})}, \tag{265}$$

with $\widehat{\mathcal{O}}(0) = 1$. This is a rate-overlap factor associated with a local short-distance transition kernel, not a complete transition-amplitude calculation.

For a normalized Gaussian effective density,

$$\rho_W(\mathbf{x}) \propto \exp\left(-\frac{\mathbf{x}^2}{2\sigma_W^2}\right), \qquad \widehat{\mathcal{O}}(d) = \exp\left(-\frac{d^2}{4\sigma_W^2}\right). \tag{266}$$

The parameter $\sigma_W$ denotes the spatial width of the effective constituent density rather than a hard classical radius.

The overlap ratio is therefore

$$\frac{\widehat{\mathcal{O}}_X}{\widehat{\mathcal{O}}_Z} = \exp\left[-\frac{d_X^2 - d_Z^2}{4\sigma_W^2}\right] \simeq \exp\left(-\frac{2.29 r_W'^2}{\sigma_W^2}\right). \tag{267}$$

The total width also depends on the transition dynamics. Schematically,

$$\Gamma_n \simeq \mathcal{K}_n \widehat{\mathcal{O}}(d_n), \qquad \frac{\Gamma_X}{\Gamma_Z} \simeq \frac{\mathcal{K}_X}{\mathcal{K}_Z}\frac{\widehat{\mathcal{O}}_X}{\widehat{\mathcal{O}}_Z}, \tag{268}$$

where $\mathcal{K}_n$ collects effective couplings, spin-dependent transition factors, accessible final states, and phase-space contributions.

As a pure-overlap benchmark, setting $\mathcal{K}_X/\mathcal{K}_Z \simeq 1$ and matching the reference-width ratio gives

$$\exp\left(-\frac{2.29 r_W'^2}{\sigma_W^2}\right) \simeq \frac{1}{609}, \qquad \frac{\sigma_W}{r_W'} \simeq \sqrt{\frac{2.29}{\ln 609}} \simeq 0.60. \tag{269}$$

Within this benchmark, the extended $X_1^0(125)$ configuration has a smaller short-distance density overlap than the compact $Z^0$ configuration. The value $\sigma_W \simeq 0.60 r_W'$ is a matching result obtained from the reference width ratio rather than an independent prediction.

The use of a short-distance overlap factor is analogous to the wavefunction-at-the-origin organization of heavy-quarkonium annihilation rates [44]. A microscopic $W^+W^-$ calculation must determine the state-dependent wavefunctions, transition operators, spin factors, couplings, phase spaces, and in particular $\mathcal{K}_X/\mathcal{K}_Z$. The Gaussian estimate therefore provides a phenomenological consistency check rather than an independent prediction of either total width.

## C Formation-Time Consistency of the Composite Interpretation

The neutral composite interpretation must also be compatible with the finite lifetime of the charged weak boson. The measured isolated-$W$ width is [15]

$$\Gamma_W = 2.085 \pm 0.042\,\text{GeV}. \tag{270}$$

For two independently decaying constituents, the probability that both survive decreases with the approximate rate

$$\Gamma_{WW}^{\text{surv}} \simeq 2\Gamma_W, \qquad \tau_{WW}^{\text{surv}} \simeq \frac{\hbar}{2\Gamma_W} \simeq 1.58 \times 10^{-25}\,\text{s}. \tag{271}$$

This is a reference independent-decay estimate; binding and channel-coupling effects may modify the constituent-decay behavior inside the neutral configuration.

A characteristic binding-response time for a neutral level $n$ may be estimated dimensionally as

$$\tau_{\text{form}}^{(n)} \sim \frac{\hbar}{\left|U_{\text{binding}}^{(n)}\right|}. \tag{272}$$

This is a timescale estimate associated with the binding-energy scale rather than a microscopic formation time derived from the full transition amplitude.

Using the effective binding energies extracted from the mass relations [15, 26],

$$\begin{aligned} \left|U_{\text{binding}}^{(Z)}\right| &\simeq 69.550\,\text{GeV}, & \tau_{\text{form}}^{(Z)} &\simeq 9.46 \times 10^{-27}\,\text{s}, \\ \left|U_{\text{binding}}^{(X)}\right| &\simeq 35.538\,\text{GeV}, & \tau_{\text{form}}^{(X)} &\simeq 1.85 \times 10^{-26}\,\text{s}. \end{aligned} \tag{273}$$

The resulting hierarchy is

$$\tau_{\text{form}}^{(Z)} < \tau_{\text{form}}^{(X)} \ll \tau_{WW}^{\text{surv}}, \tag{274}$$

with

$$\frac{\tau_{WW}^{\text{surv}}}{\tau_{\text{form}}^{(Z)}} \simeq 16.7, \qquad \frac{\tau_{WW}^{\text{surv}}}{\tau_{\text{form}}^{(X)}} \simeq 8.5. \tag{275}$$

The characteristic binding-response scales are therefore shorter than the independent-decay survival time of an initially produced $W^+W^-$ pair. This satisfies a necessary phenomenological timing condition and shows that the finite isolated-$W$ lifetime does not by itself exclude a rapidly developing short-distance $W^+W^-$ correlation.

This estimate does not establish a bound-state or resonance pole. A microscopic treatment must calculate the production and formation amplitudes, finite constituent widths, channel mixing, final-state couplings, and the complex pole structure. The present hierarchy is only a consistency check that constituent decay is not parametrically faster than the proposed binding response.

## References


[1] S. L. Glashow, "Partial-Symmetries of Weak Interactions," *Nucl. Phys.* **22**, 579–588 (1961).

[2] S. Weinberg, "A Model of Leptons," *Phys. Rev. Lett.* **19**, 1264–1266 (1967).

[3] A. Salam, "Weak and Electromagnetic Interactions," in *Elementary Particle Theory: Relativistic Groups and Analyticity, Proceedings of the Eighth Nobel Symposium*, edited by N. Svartholm (Almqvist & Wiksell, Stockholm, 1968), pp. 367–377.

[4] G. Arnison et al. (UA1 Collaboration), "Experimental Observation of Isolated Large Transverse Energy Electrons with Associated Missing Energy at $\sqrt{s} = 540$ GeV," *Phys. Lett. B* **122**, 103–116 (1983).

[5] M. Banner et al. (UA2 Collaboration), "Observation of Single Isolated Electrons of High Transverse Momentum in Events with Missing Transverse Energy at the CERN $\bar{p}p$ Collider," *Phys. Lett. B* **122**, 476–485 (1983).

[6] G. Arnison et al. (UA1 Collaboration), "Experimental Observation of Lepton Pairs of Invariant Mass around 95 GeV/$c^2$ at the CERN SPS Collider," *Phys. Lett. B* **126**, 398–410 (1983).

[7] P. Bagnaia et al. (UA2 Collaboration), "Evidence for $Z^0 \to e^+e^-$ at the CERN $\bar{p}p$ Collider," *Phys. Lett. B* **129**, 130–140 (1983).

[8] F. J. Hasert et al. (Gargamelle Collaboration), "Observation of Neutrino-Like Interactions without Muon or Electron in the Gargamelle Neutrino Experiment," *Phys. Lett. B* **46**, 138–140 (1973).

[9] G. Aad et al. (ATLAS Collaboration), "Observation of a New Particle in the Search for the Standard Model Higgs Boson with the ATLAS Detector at the LHC," *Phys. Lett. B* **716**, 1–29 (2012).

[10] S. Chatrchyan et al. (CMS Collaboration), "Observation of a New Boson at a Mass of 125 GeV with the CMS Experiment at the LHC," *Phys. Lett. B* **716**, 30–61 (2012).

[11] F. Englert and R. Brout, "Broken Symmetry and the Mass of Gauge Vector Mesons," *Phys. Rev. Lett.* **13**, 321–323 (1964).

[12] P. W. Higgs, "Broken Symmetries and the Masses of Gauge Bosons," *Phys. Rev. Lett.* **13**, 508–509 (1964).

[13] G. S. Guralnik, C. R. Hagen, and T. W. B. Kibble, "Global Conservation Laws and Massless Particles," *Phys. Rev. Lett.* **13**, 585–587 (1964).

[14] M. E. Peskin and D. V. Schroeder, *An Introduction to Quantum Field Theory* (Westview Press, 1995).

[15] S. Navas et al. (Particle Data Group), "Review of Particle Physics," *Phys. Rev. D* **110**, 030001 (2024).

[16] L. Susskind, "Dynamics of Spontaneous Symmetry Breaking in the Weinberg–Salam Theory," *Phys. Rev. D* **20**, 2619–2625 (1979).

[17] Y. Fukuda et al. (Super-Kamiokande Collaboration), "Evidence for Oscillation of Atmospheric Neutrinos," *Phys. Rev. Lett.* **81**, 1562–1567 (1998).

[18] Q. R. Ahmad et al. (SNO Collaboration), "Direct Evidence for Neutrino Flavor Transformation from Neutral-Current Interactions in the Sudbury Neutrino Observatory," *Phys. Rev. Lett.* **89**, 011301 (2002).

[19] A. G. Riess et al. (High-Z Supernova Search Team), "Observational Evidence from Supernovae for an Accelerating Universe and a Cosmological Constant," *Astron. J.* **116**, 1009–1038 (1998).

[20] S. Perlmutter et al. (Supernova Cosmology Project), "Measurements of $\Omega$ and $\Lambda$ from 42 High-Redshift Supernovae," *Astrophys. J.* **517**, 565–586 (1999), arXiv:astro-ph/9812133.

[21] S. Weinberg, "The Cosmological Constant Problem," *Rev. Mod. Phys.* **61**, 1–23 (1989).

[22] G. Aad et al. (ATLAS and CMS Collaborations), "Measurements of the Higgs Boson Production and Decay Rates and Constraints on Its Couplings from a Combined ATLAS and CMS Analysis of the LHC $pp$ Collision Data at $\sqrt{s} = 7$ and 8 TeV," *JHEP* **08**, 045 (2016), arXiv:1606.02266 [hep-ex].

[23] A. Einstein, "Ist die Trägheit eines Körpers von seinem Energieinhalt abhängig?" *Annalen der Physik* **18**, 639–641 (1905).

[24] D. J. Griffiths, *Introduction to Electrodynamics*, 4th ed. (Cambridge University Press, Cambridge, 2017).

[25] R. P. Feynman, R. B. Leighton, and M. Sands, *The Feynman Lectures on Physics, Vol. II: Mainly Electromagnetism and Matter* (Addison-Wesley, Reading, Massachusetts, 1964).

[26] H. Choi, "The $Z^0$ and $H^0$ Bosons as the Ground and First Excited States of a $W^+W^-$ System," preprint (July 2025), doi:10.13140/RG.2.2.11793.95849, https://www.researchgate.net/publication/394115428.

[27] E. C. G. Stueckelberg, "Die Wechselwirkungskräfte in der Elektrodynamik und in der Feldtheorie der Kernkräfte. Teil II und III," *Helv. Phys. Acta* **11**, 299–328 (1938), doi:10.5169/seals-110855.

[28] H. Ruegg and M. Ruiz-Altaba, "The Stueckelberg Field," *Int. J. Mod. Phys. A* **19**, 3265–3348 (2004).

[29] B. W. Lee, C. Quigg, and H. B. Thacker, "Weak Interactions at Very High Energies: The Role of the Higgs-Boson Mass," *Phys. Rev. D* **16**, 1519–1531 (1977).

[30] H. Choi, "The Klein–Gordon–Choi Equation: A Unified Resolution of the Divergences in Quantum Gravity and QED," preprint (December 2025), doi:10.13140/RG.2.2.16090.20161, https://www.researchgate.net/publication/398285103.

[31] B. W. Lee, C. Quigg, and H. B. Thacker, "The Strength of Weak Interactions at Very High Energies and the Higgs Boson Mass," *Phys. Rev. Lett.* **38**, 883 (1977).

[32] H. Choi, "The Physical Origin of the Planck Scale Cutoff and Completion of Perturbative Quantum Gravity," preprint (November 2025), doi:10.13140/RG.2.2.25902.57925, https://www.researchgate.net/publication/397952460.

[33] H. Choi, "Matter-Only Cosmology: A Unified Origin for Inflation and Dark Energy," preprint (November 2025), doi:10.13140/RG.2.2.27940.74887, https://www.researchgate.net/publication/398004497.

[34] D. J. Griffiths and D. F. Schroeter, *Introduction to Quantum Mechanics*, 3rd ed. (Cambridge University Press, Cambridge, 2018), Sec. 3.5.3, p. 109.

[35] E. Eichten, K. Gottfried, T. Kinoshita, K. D. Lane, and T.-M. Yan, "Charmonium: The Model," *Phys. Rev. D* **17**, 3090 (1978); Erratum: *Phys. Rev. D* **21**, 313 (1980).

[36] W. Buchmüller and S.-H. H. Tye, "Quarkonia and Quantum Chromodynamics," *Phys. Rev. D* **24**, 132 (1981).

[37] E. Eichten, K. Gottfried, T. Kinoshita, J. Kogut, K. D. Lane, and T.-M. Yan, "The Spectrum of Charmonium," *Phys. Rev. Lett.* **34**, 369–372 (1975); Erratum: *Phys. Rev. Lett.* **36**, 1276 (1976).

[38] D. de Florian et al. (LHC Higgs Cross Section Working Group), *Handbook of LHC Higgs Cross Sections: 4. Deciphering the Nature of the Higgs Sector*, CERN Yellow Reports: Monographs, Vol. 2 (2017), arXiv:1610.07922 [hep-ph].

[39] R. Contino, M. Ghezzi, C. Grojean, M. Mühlleitner, and M. Spira, "Effective Lagrangian for a Light Higgs-Like Scalar," *JHEP* **07**, 035 (2013).

[40] N. D. Birrell and P. C. W. Davies, *Quantum Fields in Curved Space* (Cambridge University Press, Cambridge, 1982).

[41] H. Choi, "The Dirac–Choi Equation: Gauge-Complete Spinor Realization of the KGC Framework and Euclidean 1PI UV Finiteness," preprint (May 2026), doi:10.13140/RG.2.2.26836.77449, https://www.researchgate.net/publication/405312278.

[42] A. Quadri, "Slavnov–Taylor Identities in Spontaneously Broken Non-Abelian Effective Gauge Theories," *Proc. Steklov Inst. Math.* **309**, 240–250 (2020), arXiv:1909.02596 [hep-th].

[43] M. Asorey, L. Rachwał, and I. L. Shapiro, "Unitarity Issues in Some Higher Derivative Field Theories," *Galaxies* **6**, 23 (2018), arXiv:1802.01036 [hep-th].

[44] G. T. Bodwin, E. Braaten, and G. P. Lepage, "Rigorous QCD Analysis of Inclusive Annihilation and Production of Heavy Quarkonium," *Phys. Rev. D* **51**, 1125 (1995); Erratum: *Phys. Rev. D* **55**, 5853 (1997).

[45] ATLAS Collaboration, "A Detailed Map of Higgs Boson Interactions by the ATLAS Experiment Ten Years after the Discovery," *Nature* **607**, 52–59 (2022), arXiv:2207.00092 [hep-ex].

[46] L. D. Landau, "On the Angular Momentum of a System of Two Photons," *Dokl. Akad. Nauk SSSR* **60**, 207–209 (1948).

[47] C. N. Yang, "Selection Rules for the Dematerialization of a Particle into Two Photons," *Phys. Rev.* **77**, 242–245 (1950).

[48] ATLAS Collaboration, "Search for Diphoton Resonances in the 66 to 110 GeV Mass Range Using $pp$ Collisions at $\sqrt{s} = 13$ TeV with the ATLAS Detector," *JHEP* **01**, 053 (2025), arXiv:2407.07546 [hep-ex], doi:10.1007/JHEP01(2025)053.

[49] CMS Collaboration, "Search for a Standard Model-Like Higgs Boson in the Mass Range between 70 and 110 GeV in the Diphoton Final State in Proton–Proton Collisions at $\sqrt{s} = 13$ TeV," *Phys. Lett. B* **860**, 139067 (2025), arXiv:2405.18149 [hep-ex].

[50] CMS Collaboration, "Search for Diphoton Resonances in the Mass Range from 150 to 850 GeV in $pp$ Collisions at $\sqrt{s} = 8$ TeV," *Phys. Lett. B* **750**, 494–519 (2015), arXiv:1506.02301 [hep-ex].

[51] A. Ballestrero, E. Maina, and G. Pelliccioli, "Different Polarization Definitions in Same-Sign $WW$ Scattering at the LHC," *Phys. Lett. B* **811**, 135856 (2020), arXiv:2007.07133 [hep-ph].

[52] A. Denner, C. Haitz, and G. Pelliccioli, "NLO EW and QCD Corrections to Polarised Same-Sign $WW$ Scattering at the LHC," *JHEP* **11**, 115 (2024), arXiv:2409.03620 [hep-ph].

[53] ATLAS Collaboration, "Measurement and Interpretation of Same-Sign $W$-Boson Pair Production in Association with Two Jets in $pp$ Collisions at $\sqrt{s} = 13$ TeV with the ATLAS Detector," *JHEP* **04**, 026 (2024), arXiv:2312.00420 [hep-ex].

[54] CMS Collaboration, "Measurements of Production Cross Sections of $WZ$ and Same-Sign $WW$ Boson Pairs in Association with Two Jets in Proton–Proton Collisions at $\sqrt{s} = 13$ TeV," *Phys. Lett. B* **809**, 135710 (2020), arXiv:2005.01173 [hep-ex].

[55] ATLAS Collaboration, "Evidence for Longitudinally Polarized $W$ Bosons in the Electroweak Production of Same-Sign $W$-Boson Pairs in Association with Two Jets in $pp$ Collisions at $\sqrt{s} = 13$ TeV with the ATLAS Detector," *Phys. Rev. Lett.* **135**, 111802 (2025), arXiv:2503.11317 [hep-ex].

[56] CMS Collaboration, "Measurements of Production Cross Sections of Polarized Same-Sign $W$-Boson Pairs in Association with Two Jets in Proton–Proton Collisions at $\sqrt{s} = 13$ TeV," *Phys. Lett. B* **812**, 136018 (2021), arXiv:2009.09429 [hep-ex].

[57] D. H. Perkins, *Introduction to High Energy Physics*, 4th ed. (Cambridge University Press, Cambridge, 2000).